

The NCAR Climate System Model Global Ocean Component*

PETER R. GENT, FRANK O. BRYAN, GOKHAN DANABASOGLU, SCOTT C. DONEY, WILLIAM R. HOLLAND,
WILLIAM G. LARGE, AND JAMES C. MCWILLIAMS

National Center for Atmospheric Research,⁺ Boulder, Colorado

(Manuscript received 4 April 1997, in final form 22 September 1997)

ABSTRACT

This paper describes the global ocean component of the NCAR Climate System Model. New parameterizations of the effects of mesoscale eddies and of the upper-ocean boundary layer are included. Numerical improvements include a third-order upwind advection scheme and elimination of the artificial North Pole island in the original MOM 1.1 code. Updated forcing fields are used to drive the ocean-alone solution, which is integrated long enough so that it is in equilibrium. The ocean transports and potential temperature and salinity distributions are compared with observations. The solution sensitivity to the freshwater forcing distribution is highlighted, and the sensitivity to resolution is also briefly discussed.

1. Introduction

Over the last two or three years, scientists at the National Center for Atmospheric Research (NCAR) have been building the initial configuration of a comprehensive Climate System Model (CSM). The initial release in May 1996 consisted of an atmospheric general circulation model, CCM3, a land surface model, a sea-ice model, and a global ocean model. The purpose of this paper is to describe the global ocean model and to show the results and sensitivities when it is run in ocean-alone mode forced by the observed climatological annual cycle of atmospheric conditions. However, the freshwater surface flux needs to have a term that restores to observations in order to keep the salinity field stable, but the coefficient is quite small.

Building the NCAR CSM Ocean Model has been a collaborative effort by many members of NCAR's Oceanography Section. In designing this model, we decided to start with the widely used Geophysical Fluid Dynamics Laboratory (GFDL) MOM 1.1 z-coordinate model and incorporated two new physical parameterizations. It was clear that if the ocean model is to run in a time comparable to CCM3 at the proposed resolution of T42, then its resolution will not be eddy per-

mitting. This resolution for the CSM was chosen so that many decadal and some century runs could be achieved in a reasonable time. Thus, we decided that the ocean model should include the mesoscale eddy parameterization described in Gent and McWilliams (1990) and Gent et al. (1995). Its use results in considerable improvement in the simulations of noneddy-permitting ocean models; see Danabasoglu et al. (1994) and Danabasoglu and McWilliams (1995). It was also clear that communication between the CSM atmospheric and ocean models will be relatively frequent, and the initial configuration interacts once per simulated day. This is a much higher frequency than has been traditionally used to force and spin up global ocean models. More typically, the ocean forcing during spinup has been prescribed as interpolation between monthly means. We decided that an improved upper-ocean parameterization was necessary to accurately represent the communication of high-frequency forcing to the ocean interior and incorporated the upper-ocean boundary layer scheme described and documented in Large et al. (1994). This scheme is based on the K-profile parameterization (KPP) due to Troen and Mahrt (1986), which was originally designed for atmospheric boundary layer studies. In fact, the boundary layer schemes in CCM3 and in the CSM Ocean Model are now both based on this KPP scheme.

When the subgrid-scale parameterizations are modified to more accurately represent physical processes, they may be less able to overcome or hide shortcomings in other aspects of the model formulation. In particular, with the parameterizations described above, the model is much less dissipative and dispersion errors associated with centered advection can lead to nonphysical tracer values. The problems are most apparent in regions with

* An electronic supplement to this article may be found on the CD-ROM accompanying this issue or at <http://www.ametsoc.org/AMS>.

⁺ The National Center for Atmospheric Research is sponsored by the National Science Foundation.

Corresponding author address: Dr. Peter R. Gent, NCAR/CGD, P.O. Box 3000, Boulder, CO 80307-3000.
E-mail: gent@ucar.edu

steep topography and strong gradients in temperature and salinity, such as the Denmark Strait overflow and the Mediterranean outflow, and become more severe at higher resolution. This is a well-known problem with centered advection and led us to implement a new advection scheme. It is a third-order upwind scheme that is implemented sequentially in all three spatial directions; see Holland et al. (1998). The scheme is one of the simplest proposed by Leonard (1979), and results in a simpler context are shown in Hecht et al. (1995). This advection problem in MOM has been addressed before because it shows up at high resolution even with horizontal tracer mixing; see Gerdes et al. (1991) and Farrow and Stevens (1995). Tests with the third-order upwind scheme controlled the problem, so that these much more computationally expensive schemes were deemed unnecessary.

Several other numerical modifications were made to MOM 1.1. Only one calculation of vertical velocity from the continuity equation is performed, and it is on the tracer grid; see Webb (1995). The artificial island at the North Pole was removed to allow transpolar flow. Additional terms due to Wajsovicz (1993) are included in the viscous terms of the momentum equation. The ocean code also contains a calculation of sea-ice formation and melting that is absolutely necessary when it is run with an active sea-ice model.

2. Model equations and specification

Full details of the model equations and specification can be found in the technical note written by the NCAR Oceanography Section (1996) for the model release. This section will highlight the changes made to the standard MOM 1.1 model.

The model consists of the standard horizontal momentum, hydrostatic, and continuity equations of the primitive equations solved in spherical coordinates. The standard equations in MOM 1.1 for potential temperature θ and salinity S have been modified to incorporate the eddy parameterization of Gent and McWilliams (1990) and the KPP boundary layer scheme of Large et al. (1994). The new equation for θ is

$$\theta_t + \mathcal{L}(\theta) = R(\kappa_t, \theta) + [\kappa_v(\theta_z - \gamma_\theta)]_z + H, \quad (1)$$

with

$$\begin{aligned} \mathcal{L}(\theta) = & \left(\frac{1}{a \cos \phi} \right) \{ [(u + u^*)\theta]_\lambda + [(v + v^*)\theta \cos \phi]_\phi \} \\ & + [(w + w^*)\theta]_z. \end{aligned} \quad (2)$$

In the above equations, R is the second-order diffusion operator along isopycnals with the approximation of small isopycnal slopes; see Redi (1982), Cox (1987), and Gent and McWilliams (1990). This same approximation applied to diffusion normal to isopycnals gives the vertical diffusion term in (1). Here γ_θ is the KPP nonlocal transport term and H is the penetrative com-

ponent of solar radiation plus latent heating due to sea ice formation. The advection operator \mathcal{L} contains an additional advection by the eddy-induced transport velocity, (u^*, v^*, w^*) , which is defined by

$$\begin{aligned} u^* &= \left(\frac{\kappa_1 \rho_\lambda}{a \cos \phi \rho_z} \right)_z, & v^* &= \left(\frac{\kappa_1 \rho_\phi}{a \rho_z} \right)_z, \\ w^* &= - \left(\frac{1}{a \cos \phi} \right) \left[\left(\frac{\kappa_1 \rho_\lambda}{a \cos \phi \rho_z} \right)_\lambda + \left(\frac{\kappa_1 \cos \phi \rho_\phi}{a \rho_z} \right)_\phi \right], \end{aligned} \quad (3)$$

where ρ is the local potential density and κ_1 is the isopycnal diffusivity.

So far, the NCAR CSM Ocean Model has mostly been run at two resolutions, which we have designated $\times 2$ and $\times 3$. The finer resolution, $\times 2$, has a uniform longitudinal resolution of 2.4° . The latitudinal resolution varies with the finest grid spacing being 1.2° near the equator and at high latitudes ($>60^\circ$) and the coarsest grid being 2.3° at 20°N and 20°S . The grid varies smoothly between these extremes. The idea behind the variable latitudinal grid was to provide finer resolution near the equator where there are strong zonal jets that have small meridional scales and to have almost rectangular grid boxes in midlatitudes between 20° and 60° . The $\times 2$ resolution has 45 levels in the vertical, which are stretched in an exponential fashion. The top level is 12.5 m deep and there are four levels in the upper 50 m of the ocean. The bottom level is the thickest at about 250 m and the maximum depth of the ocean is 6 km. The results presented in this paper are obtained with this $\times 2$ resolution, the same resolution used for CSM coupled runs. The $\times 3$ resolution has a horizontal grid that is 50% coarser than the $\times 2$ and has 25 vertical levels with only three levels in the upper 50 m. We have used the coarser $\times 3$ resolution to explore the model sensitivity to the applied forcing, especially the freshwater and heat flux forcings, and to the values of the model parameters; only a few cases were run with the much more computationally expensive $\times 2$ resolution. The $\times 3$ solutions are described in Large et al. (1997).

The $\times 2$ resolution has a closed Bering Strait so that Europe, Africa, Asia, the Americas, and Greenland are one continuous landmass. The Mediterranean Sea is resolved in the $\times 2$ (not in the $\times 3$) with a widened Strait of Gibraltar. There are eight islands in the $\times 2$: Spitzbergen, Iceland, the Greater Antilles, Japan, Madagascar, Australia and New Guinea, New Zealand, and Antarctica. The bottom topography was processed in the following way. The $5'$ topographic data from the National Oceanic and Atmospheric Administration National Geophysical Data Center (Sloss 1988) were first averaged onto a horizontal grid with twice the horizontal resolution of the $\times 2$ grid. It was then smoothed five times with a local, five-point Gaussian filter and, finally, interpolated to the $\times 2$ grid. The active ocean has a minimum depth of 50 m.

The $\times 2$ model configuration is run with a horizontal

viscosity of $8 \times 10^4 \text{ m}^2 \text{ s}^{-1}$ and an isopycnal diffusivity, κ_i , of $600 \text{ m}^2 \text{ s}^{-1}$. In the ocean interior below the boundary layer, the nonlocal transports γ_θ and γ_s are zero everywhere and the background value of vertical eddy viscosity is $10 \times 10^{-4} \text{ m}^2 \text{ s}^{-1}$ and diffusivity, κ_v , is $0.3 \times 10^{-4} \text{ m}^2 \text{ s}^{-1}$. These values represent mixing due to internal wave activity. They can be enhanced by local vertical shear instability up to $50 \times 10^{-4} \text{ m}^2 \text{ s}^{-1}$ in stable or neutral stratification, and up to $1000 \times 10^{-4} \text{ m}^2 \text{ s}^{-1}$ in statically unstable regions. A quadratic drag law is applied at the bottom boundary with a drag coefficient of 10^{-3} . The model time step is usually limited by the diffusive stability limit at high latitudes because of the converging meridians near the pole. To alleviate this constraint, the horizontal viscosity and κ_i are both tapered near the North Pole. The tapering starts at about 84°N and the coefficients are both reduced to 6% of their standard values at the pole. Wajswicz (1993) has shown that additional terms in the momentum equation are necessary to ensure that solid-body rotation does not produce a torque on the fluid when the horizontal viscosity is spatially dependent. These terms are small but have been added to the momentum equation. The usual Fourier filtering in the MOM 1.1 code, which eliminates the short zonal wavelength variability in the model fields where the meridians converge, is also applied in the region north of 84°N . The artificial island at the North Pole in MOM 1.1 has been removed and the pole is treated consistently as a tracer point of the model Arakawa B grid by considering it as a circular grid point.

The isopycnal diffusivity κ_i is also tapered toward zero in two additional situations. The first is done for purely numerical reasons when the isopycnal slope gets large. In MOM 1.1, a maximum slope approach was implemented to overcome the timestep limit in the explicit part of implementing the diffusion along isopycnals. However, this implies mixing across isopycnals when they are steep. An alternative approach is to reduce the diffusivity κ_i when the isopycnals are steep but ensure that the diffusion is still along isopycnals, and this is what has been implemented. The multiplying factor is one for isopycnal slopes less than 10^{-2} and decreases to zero in the limit of vertical isopycnal surfaces.

Steep isopycnal surfaces mostly occur in the upper, mixed layer of the ocean. This is where the KPP boundary layer parameterization applies. The boundary layer scheme specifies strong vertical mixing in the upper ocean, which is in direct opposition to the eddy parameterization scheme that is trying to flatten isopycnals and reduce the potential energy. This latter parameterization really only applies in the stably stratified part of the ocean below the boundary layer. The important boundary layer motions are accounted for in the KPP scheme by enhancements of the vertical mixing coefficients. Thus, when the boundary layer is resolved and explicitly handled in the ocean model, it is appropriate to turn off the eddy parameterization near the surface.

At every model grid point, the ratio of the depth to the local isopycnal slope multiplied by the radius of deformation is calculated. The second factor, which modifies the isopycnal diffusivity κ_i is a function of this ratio when both are in the range zero to one and is one otherwise. The deformation radius is not calculated from the model but is specified as a decreasing function of latitude, varying from 100 km at the equator to 15 km at the poles. Full details of the two taperings of κ_i are given in appendix B of Large et al. (1997).

In the boundary layer the KPP scheme matches the interior mixing at the base and is consistent with similarity theory near the surface, with turbulent transport vanishing at the surface. The eddy coefficients are proportional to the wind speed and to the boundary layer depth. Their maxima are typically found at about one-third this depth, where they can exceed $1000 \times 10^{-4} \text{ m}^2 \text{ s}^{-1}$. Such large mixing coefficients are handled in the model by the MOM 1.1 implicit vertical mixing scheme, modified to deal with the nonlocal term in (1). The boundary layer depth is diagnosed as the deepest penetration that boundary layer eddies formed near the surface can achieve in the presence of the vertical shear and stratification. It can extend well into subsurface stratification under certain forcing conditions. Specifically, this depth is where a bulk Richardson number first reaches a critical value of 0.3. This parameter and all other KPP parameter values are independent of position, so that the scheme works the same way for equatorial, midlatitude, and polar ocean boundary layers. This is similar to atmospheric applications where the critical Richardson number has varied from 0.25 in the fine vertical resolution model of Holtslag et al. (1990) to 0.5 in the coarser Troen and Mahrt (1986) configuration. Turbulent shear contributes to this diagnosis, to make the entrainment of buoyancy independent of the interior stratification under purely convective forcing. A full description of the KPP scheme is found in Large et al. (1994).

In order to overcome numerical dispersion errors caused by the centered advection scheme in MOM 1.1, a sequential application of a third-order upwind scheme in the three spatial directions was implemented; see Holland et al. (1998). The time scheme for the tracer equations is still leapfrog and not forward in time as implemented in MOM by the FRAM group; see Farrow and Stevens (1995). This scheme and variants are fully discussed in Leonard (1979) and Hecht et al. (1995). This advection scheme increases the computational cost of the model by about 10% and controls extrema adequately, so that more expensive schemes were deemed unnecessary. This advection scheme has not been generally used for the $\times 3$ resolution.

3. Surface forcing and running

The uncoupled NCAR CSM Ocean Model is forced in a similar manner as when it is coupled to an atmo-

spheric model. The open-ocean surface boundary conditions are fluxes of momentum, heat, and freshwater. In areas of sea ice, more traditional boundary conditions of strong restoring to observed temperature and salinity are used.

The open-ocean turbulent heat fluxes are computed from a prescribed atmospheric state using traditional, bulk formulas. The required surface winds, air temperature, and air humidity are obtained from the National Centers for Environmental Prediction (NCEP) global reanalysis dataset; see Kalnay et al. (1996). In addition, cloud fraction from Rossow and Schiffer (1991) and surface insolation from the International Satellite Cloud Climatology Project (ISCCP) are used. A constant ocean albedo of 7% is applied to the downward shortwave flux, which is allowed to penetrate below the ocean surface. The subsurface profile allows one-third of the flux to penetrate with an e -folding scale of 17 m. Calculations using the sea surface temperature climatology of Shea et al. (1990) and the above fields led to a net ocean heat input of nearly 50 W m^{-2} in global average. This was nearly eliminated by reducing the surface insolation to 87.5% of the ISCCP values and by decreasing the NCEP reanalyzed air humidity by 7%. This last adjustment also increases the evaporation from the ocean surface by about 15%. Full details of these adjustments are given in appendix A of Large et al. (1997).

The net ocean freshwater flux also requires an estimate of precipitation. Monthly estimates were computed from the Microwave Sounding Unit (MSU) data; see Spencer (1993). There is considerable uncertainty in these estimates and the equilibrium values of sea surface salinity are very sensitive to the forcing because it has no local feedback on the freshwater flux. To overcome this, we allowed two modifications to the freshwater flux. The first was to multiply the precipitation P by a factor, f , that made the globally averaged P balance the globally averaged evaporation E . The second was to have a local restoring term to observed salinity that has zero global mean and as long a restoring timescale as possible. Thus the open-ocean freshwater flux is given by

$$\begin{aligned} F &= fP - E + F_w - \langle F_w \rangle, \\ F_w &= -\Gamma_F(S_L - S_1). \end{aligned} \quad (4)$$

Angle brackets denote a global open ocean average, S_L is the average over the upper 50 m from the Levitus (1982) seasonal climatology, and S_1 is the salinity of the first layer. Here Γ_F is inversely proportional to the restoring timescale, which, for the $\times 2$ configuration, was chosen to be 6 months over 50 m; see section 7. The restoring term is one method in ocean-alone runs of incorporating the effects of river runoff and exchanges with marginal seas that are not incorporated in the active model domain.

In the ocean-alone spinup, sea ice is diagnosed to occur where the Shea et al. (1990) monthly climatology

indicates an SST of -1.8°C . Both the heat and freshwater fluxes under ice are specified by strongly restoring the model surface layer temperature and salinity to climatology with an effective timescale of 6 days for a 50-m mixed layer. The SST climatology used is that of Shea et al. (1990) and the salinity climatology is the upper 50-m average from Levitus (1982). This strong relaxation forces the ocean model surface temperature and salinity to closely follow the observations but results in unrealistically noisy flux fields under ice. We decided to force the ocean model in this way, although having an active sea ice model as part of the spinup may be preferable. The open-ocean and under-ice fluxes are linearly blended through a transition region where the Shea et al. (1990) climatology gives an SST between -0.8° and -1.8°C . Strong restoring is also used in the Mediterranean because of a lack of forcing data in this region.

The wind stress forcing the ocean model depends only upon the NCEP reanalyzed surface wind and a climatological SST, so that the stability dependence of the drag coefficient is taken into account. The ocean is forced by linearly interpolating between midmonthly stress values, and the annual average wind stress is shown in Fig. 1. The zonal component has maxima of about 0.1 N m^{-2} in the North Atlantic, North Pacific, and South Indian Oceans, and a maximum of about 0.2 N m^{-2} in the region $70^\circ\text{--}90^\circ\text{E}$ between 45° and 60°S . The zonal average of the zonal component has a maximum of 0.14 N m^{-2} in this last region. The meridional wind stress also has a familiar pattern. Strong northward stresses occur in the northern oceans, in eastern basins in the Southern Hemisphere, and off Antarctica. The strongest southward stresses are in the northern tropics and in the Southern Hemisphere between 45° and 60°S . Note that the atmosphere–ocean stress is applied without modification in regions diagnosed to be covered by sea ice.

The initial conditions for the $\times 2$ configuration were interpolated from an equilibrium solution of the $\times 3$ version that had been forced in exactly the same way, except that the open-ocean salinity restoring timescale was 2 yr. A run of the $\times 2$ configuration with a 2-yr restoring time will be described in section 7. However, the 6-month restoring time was chosen because it made the $\times 2$ equilibrium solution not very different from the $\times 3$ solution. The $\times 2$ equilibrium solution was obtained by running the model using the acceleration technique of Bryan (1984), which consists of two parts. The time step used for the surface θ and S calculation is 10 times that used in the momentum equation, and the deep θ and S time step is 10 times that used for θ and S in the upper 1 km. At the end of each year, the precipitation factor f was adjusted by calculating the annual volume-integrated freshwater tendency over the previous year. Then the precipitation is reduced or enhanced if the ocean salinity decreased or increased over the previous year.

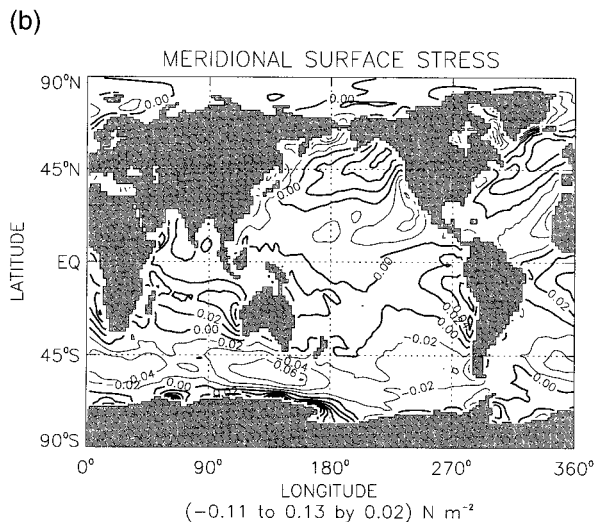
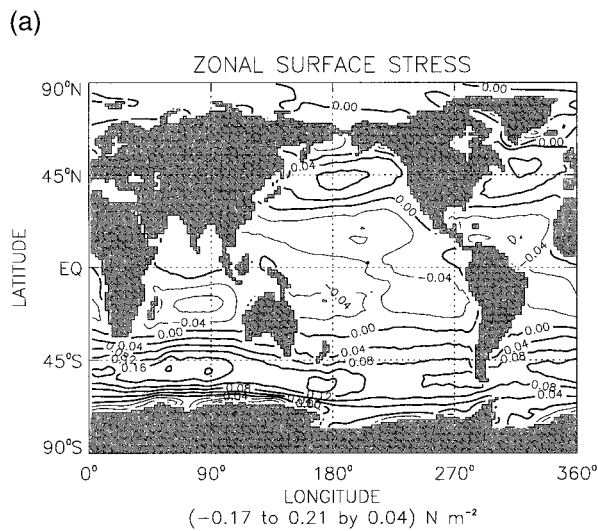


FIG. 1. The NCEP reanalyzed annual average wind stress in $N\ m^{-2}$. (a) Zonal component and (b) meridional component.

The open-ocean salinity restoring term equilibrates very slowly in this spinup and takes nearly 400 upper-ocean tracer years before it reaches its equilibrium value. This means that the precipitation factor is also changing very slowly during this period. The $\times 2$ model was run for a further 160 upper-ocean tracer years in accelerated mode. The value of f over the last year was calculated to be 1.087. Thus, the $\times 2$ model uses a precipitation increased by 8.7% over the MSU data. The precipitation factor was then kept constant and the model run for a further 17 yr in synchronous mode where all the timesteps are equal. There is no acceleration used in this phase of the spinup; see Danabasoglu et al. (1996), where this technique is shown to work well in determining an equilibrium solution. The upper-ocean θ and S adjust somewhat during the synchronous run and would adjust further if the model were run longer.

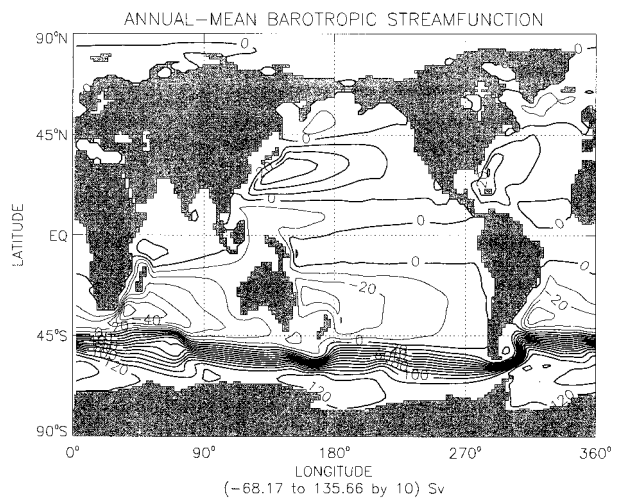


FIG. 2. The time average barotropic streamfunction in Sverdrups.

At the end the average net heat flux is $0.05\ W\ m^{-2}$ and net water flux is $3\ mm\ yr^{-1}$. However, the further adjustment would be very small compared to model errors in θ and S , and further costly synchronous integration is not justified. Full details of the material in this section can be found in the technical note of the NCAR Oceanography Section (1996).

4. Equilibrium time-averaged solution

The annual average barotropic streamfunction for the equilibrium state is shown in Fig. 2. The barotropic streamfunction is calculated from the Eulerian mean velocity and has a maximum positive value of 135 Sv ($1\ Sverdrup \equiv 10^6\ m^3\ s^{-1}$, Sv) near $0^\circ E$ longitude to the south of the Antarctic Circumpolar Current (ACC). The mass transport of the ACC is somewhat dependent on the value of isopycnal diffusivity, which was partially tuned to obtain an ACC transport through Drake Passage close to the observed value of about 120 Sv. The mid-latitude gyres in both hemispheres of the Atlantic and Pacific are greater than 30 Sv. This reflects approximate Sverdrup balance and the model resolution prevents an accurate simulation of the tight recirculations in these locations. There are distinct subpolar gyres in both the Atlantic and Pacific with transports of >10 Sv. The strongest midlatitude gyre is in the southern Indian Ocean with a transport >70 Sv in the region of the Agulhas current and its retroflexion to the east of South Africa. The Indonesian passage has been artificially widened in the model, which cannot resolve at all well the islands in this region. The Indonesian throughflow has an average value of 16.7 Sv, which is within the range of observational estimates. However, the flow through the Mozambique Channel is unrealistically large compared to observations.

The meridional overturning streamfunction is calculated from the effective transport velocity because this

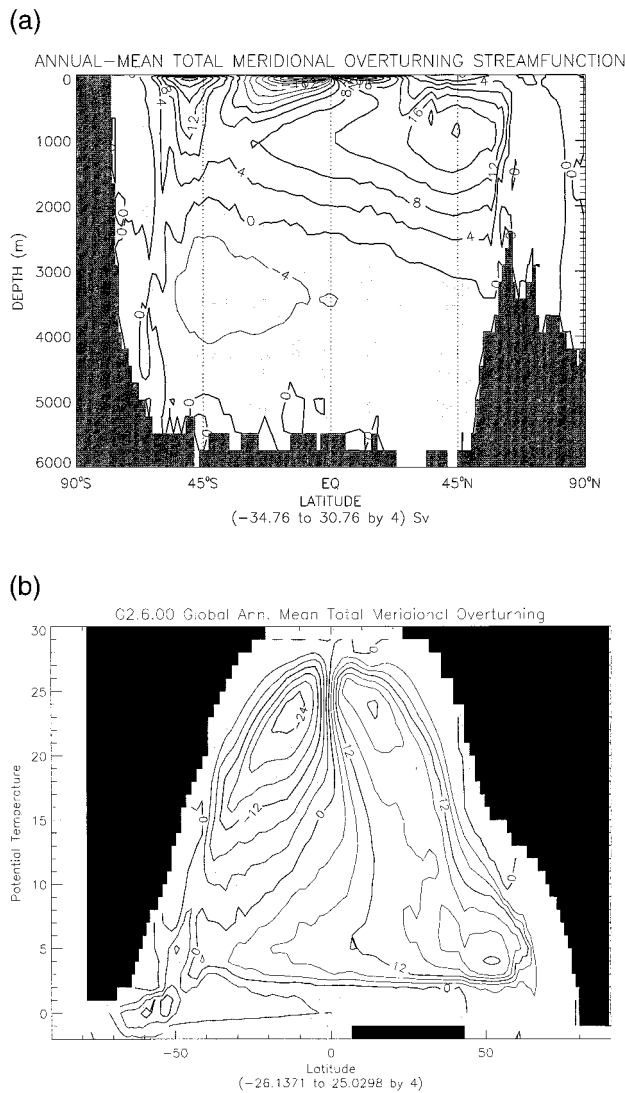


FIG. 3. The global zonally averaged meridional overturning streamfunction in sverdrups from the effective transport velocity, (a) plotted against depth and (b) plotted against potential temperature.

velocity advects the tracers; see Eq. (1). This velocity is the sum of the Eulerian mean velocity and the parameterized eddy-induced transport velocity. The streamfunction is plotted in the latitude and depth plane in Fig. 3a. The maximum positive and negative streamfunction values are 30 and -35 Sv, which occur near the surface in the Tropics. The Northern Hemisphere overturning circulation reaches a maximum of 20 Sv at 45°N at 1-km depth, and almost all of this occurs in the North Atlantic. More than 10 Sv of this circulation crosses the equator at a depth of 1 km. A perennial problem in z -coordinate, coarse-resolution models is that this overturning circulation does not go deep enough compared to observations. This model is no exception, and the circulation reaches only to 3 km at 60°N. This problem is a combination of not making

North Atlantic deep water quite in the correct locations and with the correct θ and S values, and a poor representation in the model of the overflows at Denmark Strait and east of Iceland. In the Southern Hemisphere, the overturning circulation has a maximum of 25 Sv at 50°S near the surface. This circulation is zero at 2-km depth and reverses in the deep ocean with a Southern Hemisphere overturning circulation of 7–8 Sv, which spreads Antarctic bottom water northward to fill the deep ocean below about 3 km. The overturning circulation from the Antarctic shelf is 2–3 Sv.

The component of the overturning circulation due to the eddy-induced transport velocity is less than 3 Sv everywhere except in the region of the ACC, where it reaches a maximum of -14 Sv at 55°S, 1.6-km depth. The pattern is quite similar to that shown in Fig. 7 of Gent et al. (1995), which was calculated from the Levitus (1982) observations with κ_1 modified by a first baroclinic vertical mode profile. This modification reduced the overturning near the surface in the ACC, and a similar effect is found in this model because of the tapering of κ_1 near the surface. Thus, the eddy-induced overturning does not almost cancel the overturning of the Eulerian velocity, often called the Deacon cell, in the upper kilometer of the ocean. The cancellation of the Deacon cell in this model is not as complete as that found in the earlier simulations of Danabasoglu et al. (1994) and Danabasoglu and McWilliams (1995), which had no tapering of κ_1 and used different forcing fields. We believe the present simulation has a more realistic overturning circulation in this region.

The meridional overturning streamfunction in the latitude and potential temperature plane is shown in Fig. 3b. This coordinate system emphasizes the overturning in the upper tropical oceans, which occurs in both hemispheres at an average temperature of 25°C. A maximum of 24 Sv of water is transported to the south in the deep western boundary current of the North Atlantic at a potential temperature of 3°–4°C, which is slightly warmer than in reality; see Molinari et al. (1992). This probably contributes to the North Atlantic overturning not going deep enough. The overturning on the Antarctic shelf in the model is at 0°C and this water mass spreads northward to fill the deep ocean.

The meridional transports across several latitude circles in the Atlantic Ocean for four potential temperature layers are shown in Fig. 4. The temperatures used to define the layers in the CSM model are 7° (SW), 4° (IW), 1° (DW), and -2° (BW). They were chosen because they correspond to the depths used by Macdonald and Wunsch (1996) to make a similar calculation from their global box inverse model. The corresponding results from Macdonald and Wunsch are also plotted in Fig. 4. In both models, virtually all of the overturning in the Northern Hemisphere occurs in the North Atlantic basin. The models are in close agreement over most of the North Atlantic with 15–18 Sv of warm surface-layer water moving northward compensated for primarily by

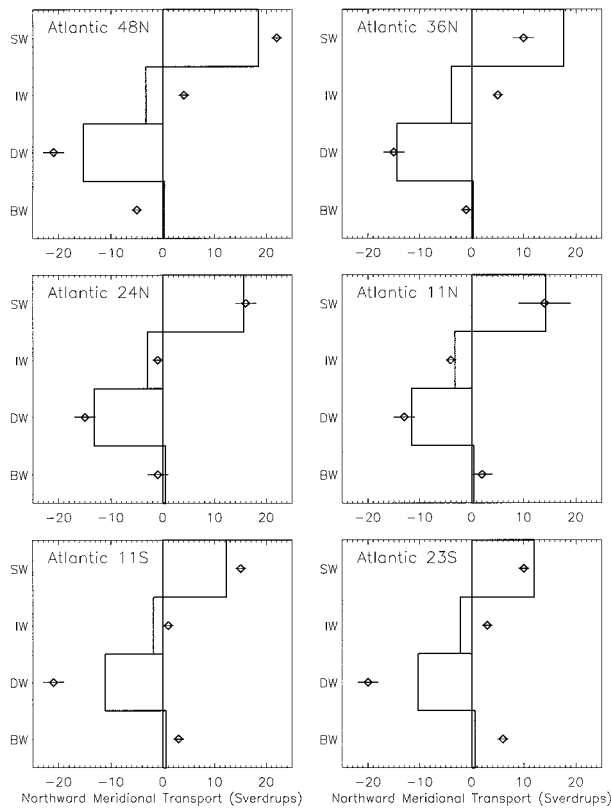


FIG. 4. Northward meridional transport in Sverdrups in the surface, intermediate, deep, and bottom water layers across zonal sections of the Atlantic Ocean at the indicated latitudes. The results of the Macdonald and Wunsch (1996) global box inverse model are the diamond symbols, along with their error estimates.

southward transport in the deep water layer. At the southernmost sections in the Atlantic, the CSM model predicts slightly weaker southward transport of deep water and northward transport of bottom and intermediate waters than does the inverse model. The models do not agree as well in the Indian and Pacific basins, where the overturning circulation is much weaker; see Fig. 5. In particular, the CSM model predicts much weaker inflow of 3 Sv into the deep Indian basin at 32°S than the 18 Sv in the inverse model. However, there is considerable dispute over the correct value for this quantity. Lee and Marotzke (1997) fit a general circulation ocean model to data and find the most consistent results when the deep inflow is 2 Sv across 32°S in the Indian Ocean. The Macdonald and Wunsch (1996) inverse model shows strong northward bottom water flow and southward deep water flow at 10°N in the Pacific. Instead, the CSM model predicts very weak meridional transport in all layers at 10°N. The CSM model predicts northward transport in all potential temperature layers across 28°S in the Pacific, whereas the inverse model has a somewhat weaker northward flow at this latitude. The CSM northward net transport is largely compensated for by the Indonesian Throughflow and southward

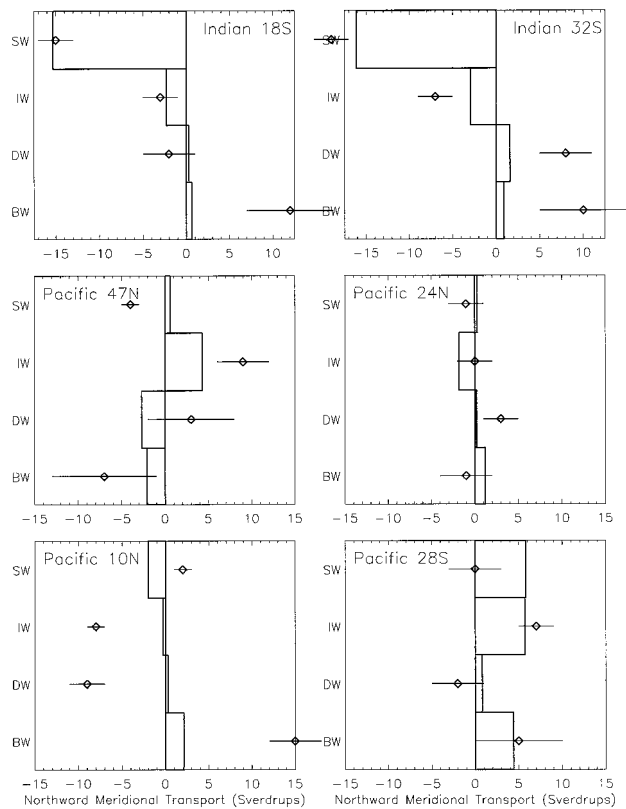


FIG. 5. The same as Fig. 4 but for the Indian and Pacific Oceans.

transport in the surface layer of the Indian Ocean. This result is consistent with the CSM model barotropic throughflow of 16.7 Sv mentioned above, compared to the considerably weaker throughflow strength of 11 Sv in the inverse model. The range of observational estimates of the throughflow strength encompasses both these values, but the CSM model value may be a little high.

Figure 6 shows the average surface velocity from the simulation. The maximum zonal velocity is 55 cm s⁻¹ westward in the middle of the equatorial Pacific. In the equatorial Atlantic, the maximum is about 30 cm s⁻¹, and a fairly strong current flows to the northwest along the coast of South and Central America into the Gulf of Mexico. The maximum eastward zonal velocity is 25 cm s⁻¹, which occurs just off South America in Drake Passage. The ACC zonal surface velocity averages between 10 and 15 cm s⁻¹ around the globe. The fastest meridional surface velocities are all in western boundary currents, with the extrema being 27 and -35 cm s⁻¹ east of southern South America and off southeast Africa, respectively. These surface velocities are certainly limited by the coarse model resolution, and the maximum values would increase quite strongly as a function of higher resolution. Similarly, the lateral scale of many of the currents, especially the equatorial current systems, is too broad and would decrease with increasing resolution.

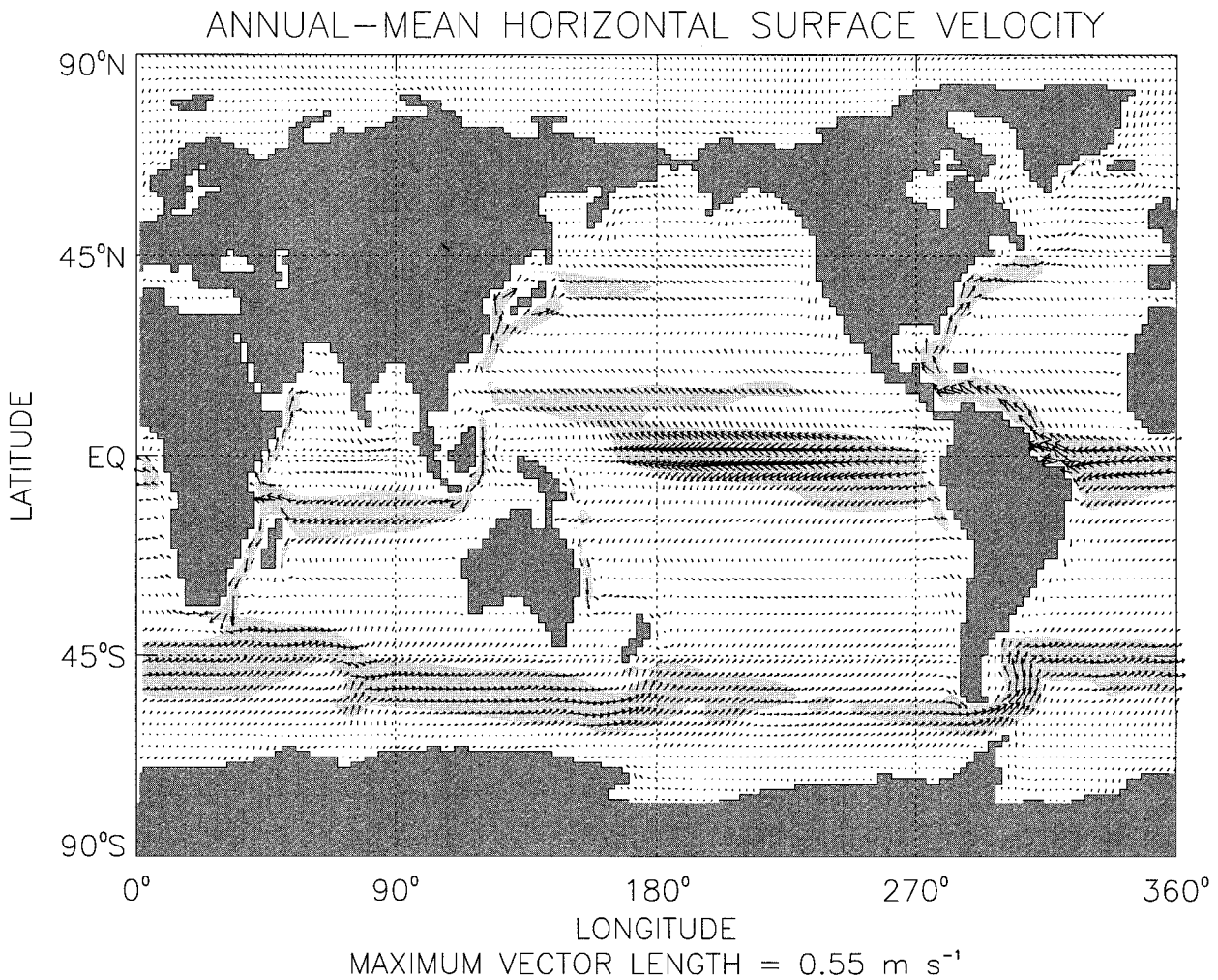


FIG. 6. Time average ocean surface velocity (m s^{-1}). Areas greater than 0.1 m s^{-1} are shaded.

Figure 7 shows the model horizontal velocity at a depth of about 2.5 km, which is the depth of the strongest middepth currents in the Atlantic Ocean. They are clear in Fig. 7, returning deep water formed in the north along the western side of the basin. The deeper part of the ACC also shows up clearly in the figure, and the maximum speeds at this depth are $3\text{--}4 \text{ cm s}^{-1}$. Figure 8 shows the horizontal velocity at a depth of 3.8 km, where the maximum speed is about 1 cm s^{-1} . The figure shows the deep water formed off Antarctica spreading northward in both the Atlantic and Pacific Oceans. At this depth the flows hug the east side of the topography, and there is significant flow in both the central Atlantic and Pacific Oceans.

The difference between the annual average surface temperature and the climatology of Shea et al. (1990) is shown in Fig. 9a. The SST differences are quite small because of the nature of the bulk heat flux forcing, which has negative feedbacks that reduce perturbations. In addition, the adjustments to the observed atmospheric variables described above were made to ensure a bal-

anced heat budget using the Shea et al. (1990) SST climatology. Thus, there can be local and seasonal errors in the SST, but the global, annual average SST in the equilibrium state is constrained to be close to the climatology. The cold bias in the central equatorial Pacific is partly attributable to the smoothness of the climatology, which is too warm in this location. Elsewhere, the largest differences are all in regions of very strong SST gradients. The differences reflect small displacements in the location of the model ACC, Kuroshio, and Gulf Stream. The largest differences occur west of Iceland and north of western Russia at 40°E .

Figure 9b shows the difference between the model annual average surface salinity and the Levitus (1982) surface climatology. The surface salinity compares well with the climatology in most open-ocean areas. The subtropical maxima in all oceans are realistic, and the asymmetry of the high-latitude salinity distributions in the North Atlantic and North Pacific responsible for maintaining the conveyor belt circulation is well represented. Many of the largest model errors are located

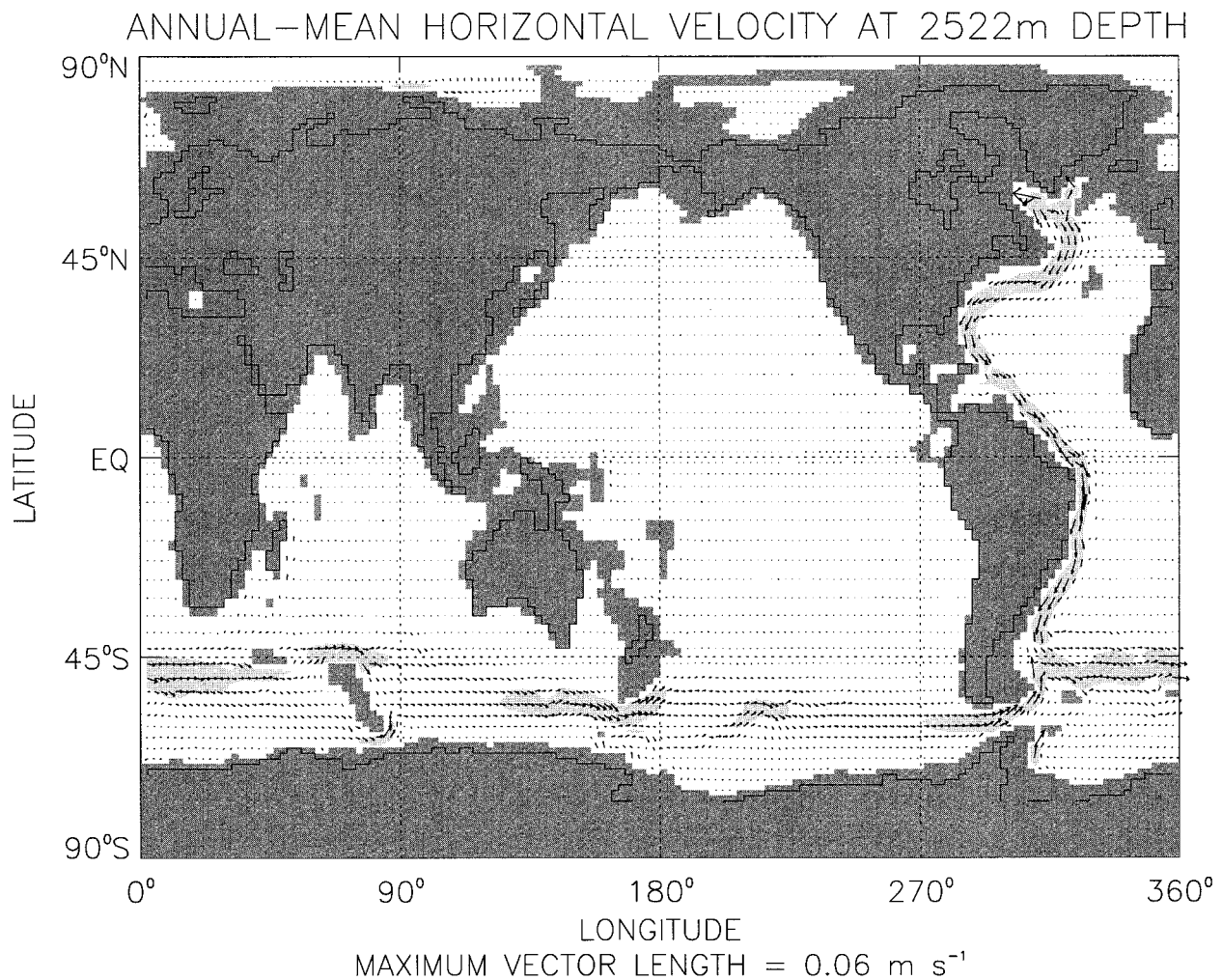


FIG. 7. Time average horizontal velocity at a depth of 2522 m (m s^{-1}). Areas greater than 0.01 m s^{-1} are shaded.

near the mouths of major rivers, such as the Amazon, Congo, Mississippi, Plata, Ganges, MacKenzie, and Yangtze, where the model solution is consistently too salty. The remaining large errors are located in the Gulf Stream region, in the Arctic and in marginal seas, for example, Hudson Bay. There is a very strong surface halocline in the Arctic, so that most of the error here is because the model is restored to the 50-m average value, and Fig. 9b is calculated using the Levitus surface value. In sharp contrast to the strong negative feedbacks in the surface heat flux, there are no local feedbacks from surface salinity on either the heat or freshwater flux. This means that the surface salinity can drift slowly, but inexorably, over long runs that are trying to reach an equilibrium solution. In the end, the surface salinity does change the thermohaline overturning circulation by affecting deep water formation, but this timescale is hundreds of years. This lack of salinity feedback is why the local restoring term is needed in the freshwater forcing given by Eq. (4). Even if precipitation globally balances evaporation, but this term is absent, then the mod-

el slowly but surely deviates from the Levitus observations as it is integrated forward in time. This aspect of the model will be discussed more fully in section 7.

Figure 10 shows the mean vertical potential temperature profile for the global ocean and various ocean domains from the model and the Levitus (1982) climatology. Figure 10a shows a slightly more diffuse main thermocline than is observed. However, this long-standing problem with global z -coordinate models has been considerably reduced by incorporating the mesoscale eddy parameterization and by using small values of κ_v in Eq. (1). This problem could be further alleviated by using a smaller value of κ_v than $3 \times 10^{-5} \text{ m}^2 \text{ s}^{-1}$, which is still larger than estimates from open-ocean observations; see Ledwell et al. (1993). Below 2 km, the model is colder than observations in the global mean, with a maximum error of 0.5°C in the deep ocean where the Levitus data give 1°C and the model gives 0.5°C . Figure 10b shows that in the Arctic the model is uniformly 1°C colder than observed and that the potential temperature maximum associated with the Atlantic in-

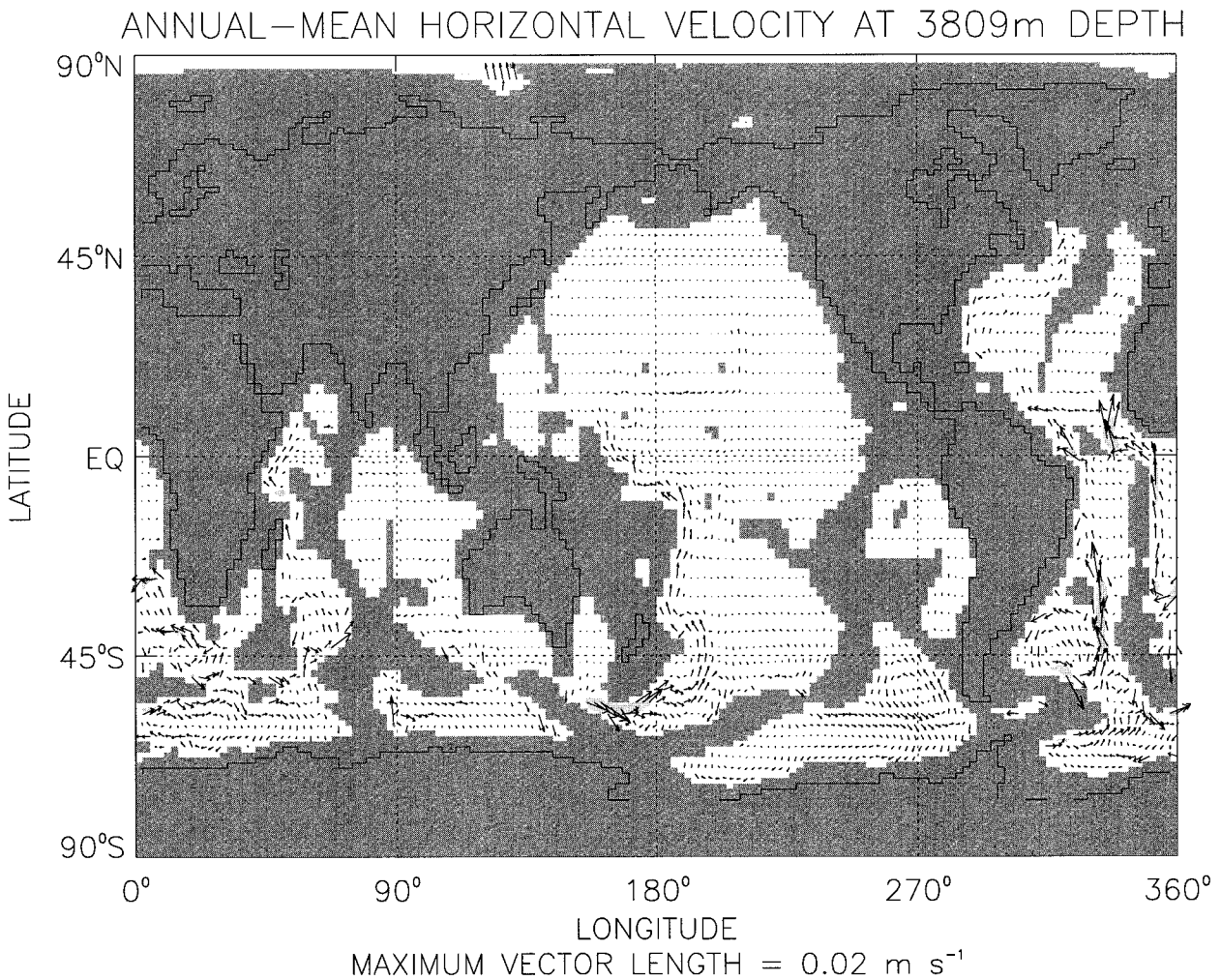


FIG. 8. Time average horizontal velocity at a depth of 3809 m (m s^{-1}).

flow layer near 500 m is underestimated. This apparent model cold bias occurs even at the surface because the model is strongly restored to the Shea et al. (1990) SST data, which are about 1°C colder than the Levitus climatological estimate. Figures 10d–f show that the discrepancies between the model and observations in the Pacific, Indian, and Southern Oceans are similar to those in the global mean, with an overly diffuse main thermocline and a weak cold deep bias. Figure 10c shows that the model is not as good in simulating the vertical temperature structure of the Atlantic Ocean. Here the model is significantly too warm in the main thermoclinic region centered on 1 km and is considerably too cold below 3 km. The warm bias near 1 km can be partly attributed to insufficient northward penetration of relatively cool Antarctic intermediate water into the Atlantic basin. The maximum error is 2°C at a depth of 4 km. The deep cold bias is associated with the fact that the North Atlantic overturning circulation does not go deep enough, and the Atlantic below 3 km is ventilated by colder Antarctic bottom water.

The problems related to misplacement of water masses described above also show up in the model salinity vertical profiles that are compared to the Levitus (1982) climatology in Fig. 11. Figure 11c shows that the Atlantic salinity is considerably too saline in the region around 1 km and is considerably too fresh below 3 km. It is interesting how the θ and S errors compensate for each other in the Atlantic vertical profiles, so that the model vertical profile of potential density is quite close to that calculated from the Levitus climatology. The model salinity profiles also have quite large errors in the Indian and Southern Oceans. Figure 11e shows that the model is much too fresh in a region centered on 1 km in the Indian Ocean. Figure 11f shows that the model ocean is too fresh around 500 m, but is too saline between 1 and 3 km in the Southern Ocean. The high salinity in the 1–3-km layer is consistent with the shallowness of the Atlantic outflow in the model solution. The vertical salinity distribution in the Pacific agrees relatively well with the climatological distribution, except for an underestimate of the maximum near 200 m.

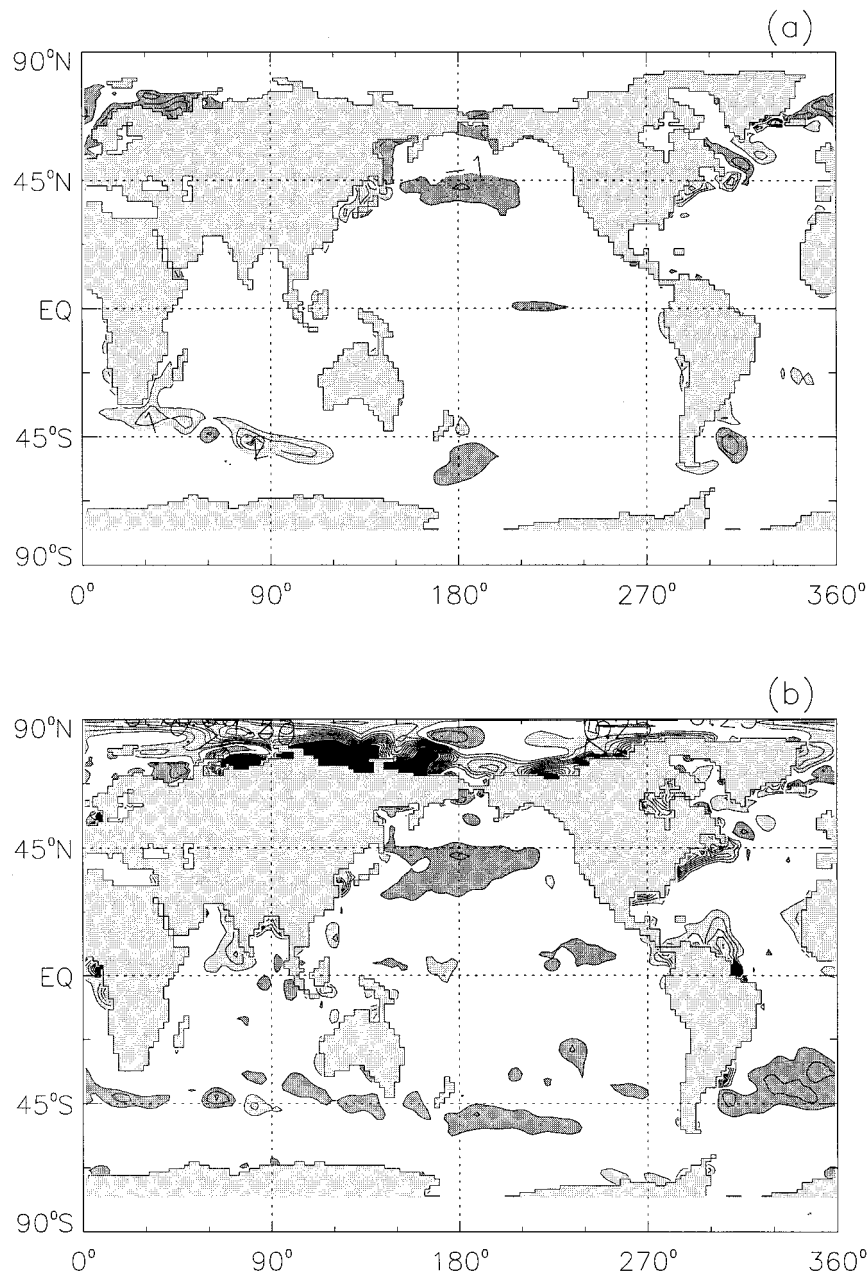


FIG. 9. (a) Time average surface potential temperature minus the climatology of Shea et al. ($^{\circ}\text{C}$), and (b) the time average surface salinity minus the climatological estimate of Levitus (ppt).

Figure 11b shows that the model captures the strong Arctic halocline quite well. Both the Levitus data and the model show very strong salinity gradients near the surface in Fig. 11b. In global average, the vertical salinity profile agrees with the climatology to within approximately 0.1 ppt at all depths.

The model simulates the salinity in the Pacific Ocean well. This is clear in Fig. 12, which shows the zonal average of salinity from the upper 1.5 km of the model Pacific; the shading gives the difference from the Levitus climatology. The figure shows that the model has

a good representation of the plume of Antarctic intermediate water in the upper kilometer of the Southern Hemisphere. This feature is much improved over simulations using strong restoring boundary conditions; see Large et al. (1997). The largest difference is that the Pacific is too fresh between 100 and 400 m in the Bering Sea, which is probably related to closing the Bering Strait in the CSM model. Figure 13 is similar to Fig. 12 except for the Indian Ocean. Again the plume of Antarctic intermediate water is well represented, and the largest errors are in the far north. There the Indian

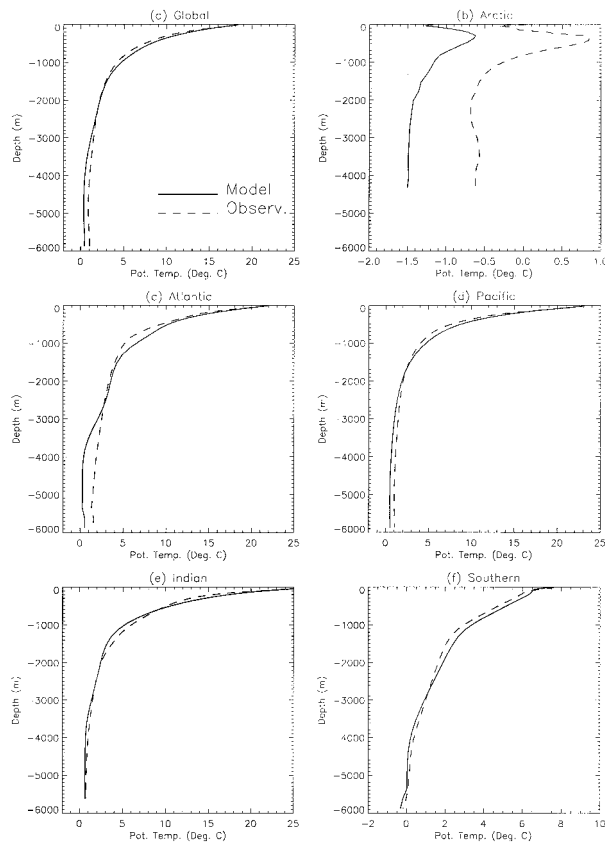


FIG. 10. Area average ocean potential temperature ($^{\circ}\text{C}$) plotted against depth from the model and the Levitus observations for the global ocean and five ocean basins.

Ocean is too saline at the surface but much too fresh in a depth range centered on 1 km. This fresh bias probably results from the absence of high salinity outflow from the Red Sea and Persian Gulf in the model.

The Mediterranean Sea is resolved in the CSM ocean $\times 2$ resolution, whereas it is absent in the $\times 3$ resolution. The surface boundary conditions in the Mediterranean are strong restoring to observations, because all the data needed in the bulk forcing are not available. Thus, the model SST and SSS errors are small in this region. The Strait of Gibraltar has been widened to two model grid points in the $\times 2$ version. Dense Mediterranean water spills over the sill and forms a tongue of salty water across the North Atlantic. However, the tongue in the model is not as deep as in reality. This is similar to the North Atlantic deep water problem mentioned above. Both are probably due to a poor representation of dense water flowing down topography in z -coordinate models.

The annual average model net surface heat and freshwater fluxes, excluding the strongly restored contributions under sea ice, are shown in Fig. 14. The heat flux in Fig. 14a shows the anticipated pattern that the ocean gains heat in the Tropics and subtropics, and loses heat farther poleward, especially off the east coasts of Asia and North America. The largest heat flux into the ocean

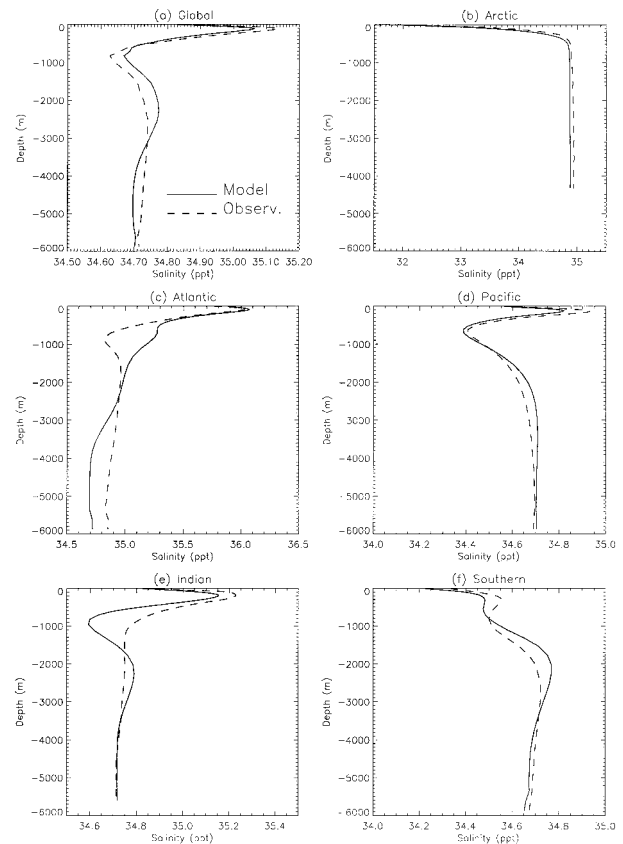


FIG. 11. The same as Fig. 10 but for salinity (ppt).

is $>110 \text{ W m}^{-2}$ on the equator between 120° and 150°W , which is where the air-sea temperature difference is quite large because of strong upwelling on the equator. The heat flux is smaller, between $\pm 40 \text{ W m}^{-2}$, over large areas of the subtropics, and near Antarctica. In the Arctic, the strong restoring gives a surface flux distribution with small horizontal scales, but the magnitude is relatively small. The areas where the ocean loses significant amounts of heat are in the western South Indian Ocean, North Pacific, and North Atlantic. The small areas of biggest heat loss, $>1000 \text{ W m}^{-2}$, are the grid boxes over the Denmark Strait and off the southern tip of Greenland. These are climatically important and sensitive areas where the ocean loses heat, North Atlantic deep water is formed, and sea ice is present for part of the year, so that the ocean also has significant freshwater sinks and sources here.

The net open-ocean freshwater flux is shown in Fig. 14b. The fluxes under sea ice in the Arctic are not shown because the strong restoring creates small-scale positive and negative bullets of up to 15 m yr^{-1} . The restoring under Antarctic sea ice produces a reasonable source of freshwater, which has also been omitted in Fig. 14b. Elsewhere, the patterns are reasonable with net freshwater sources under the intertropical and South Pacific convergence zones in the tropical Pacific and in the

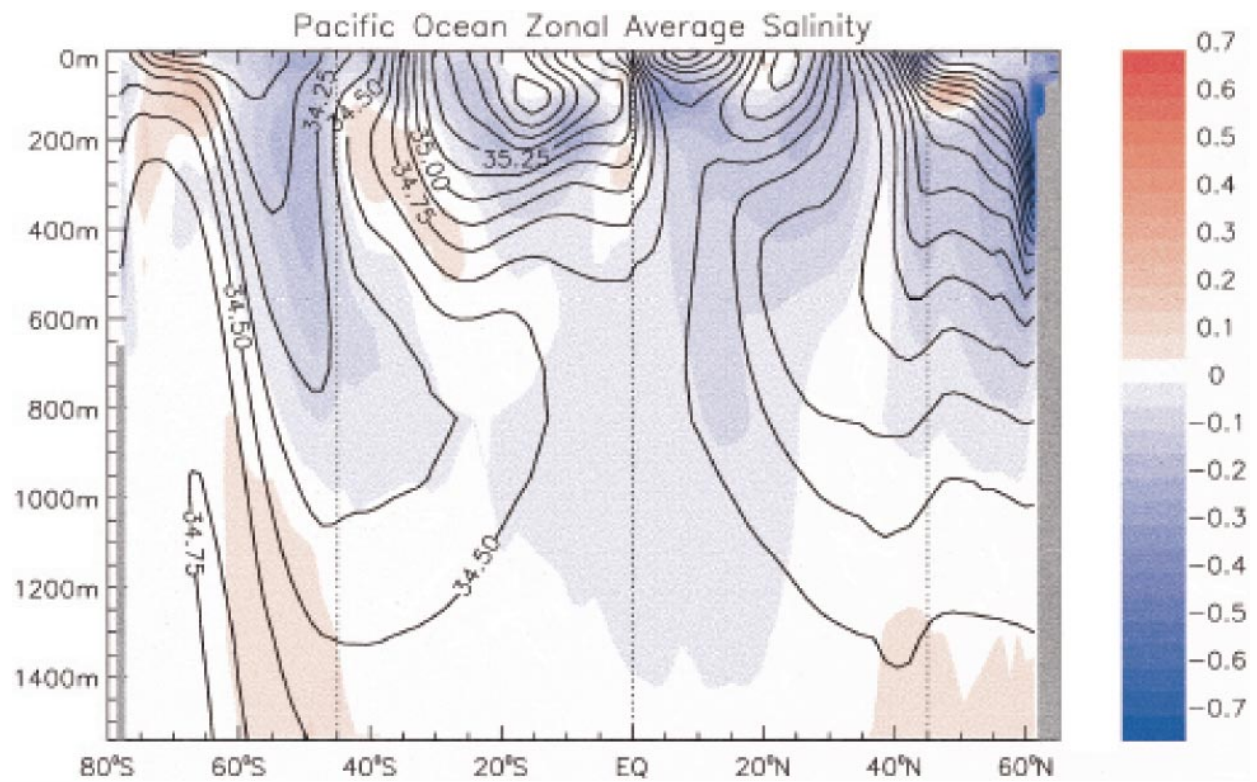


FIG. 12. The zonally averaged salinity from the upper 1.5 km of the model Pacific Ocean with a contour interval of 0.125 ppt. The shading shows the difference compared to the Levitus climatology with a contour interval of 0.05 ppt.

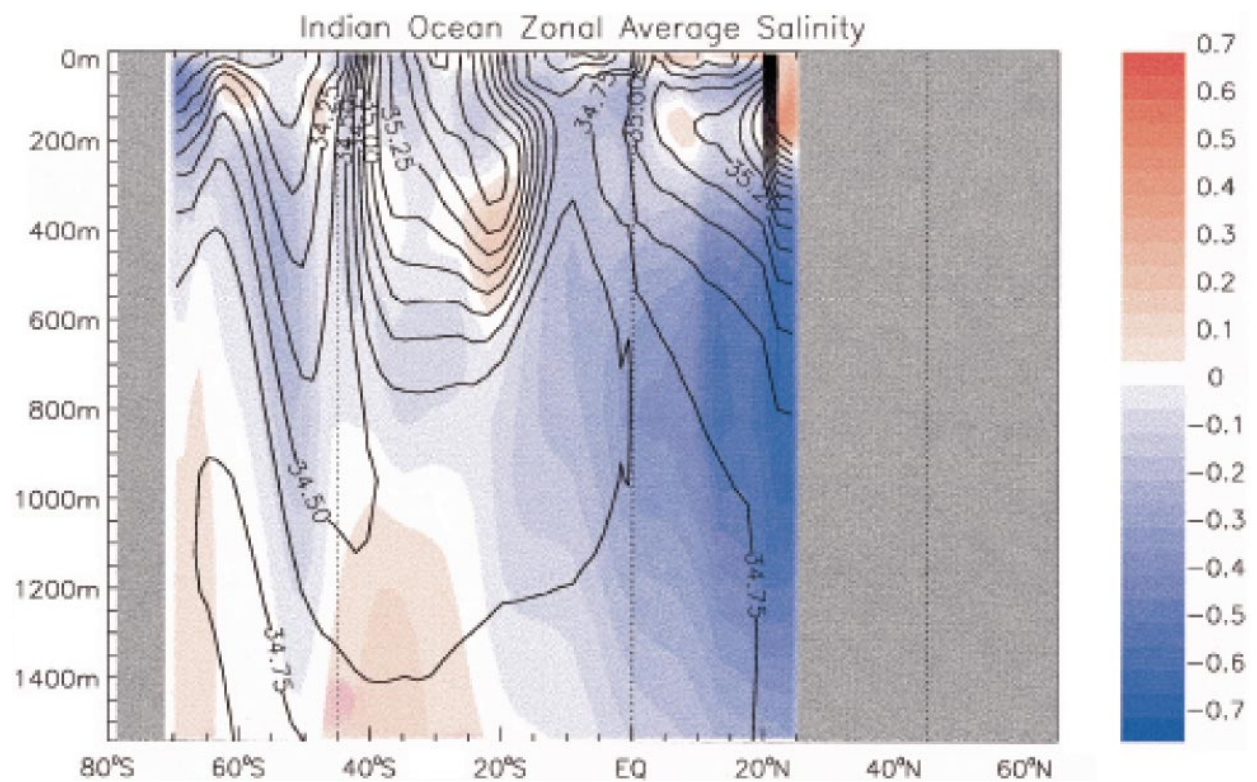


FIG. 13. The same as Fig. 12 but for the model Indian Ocean.

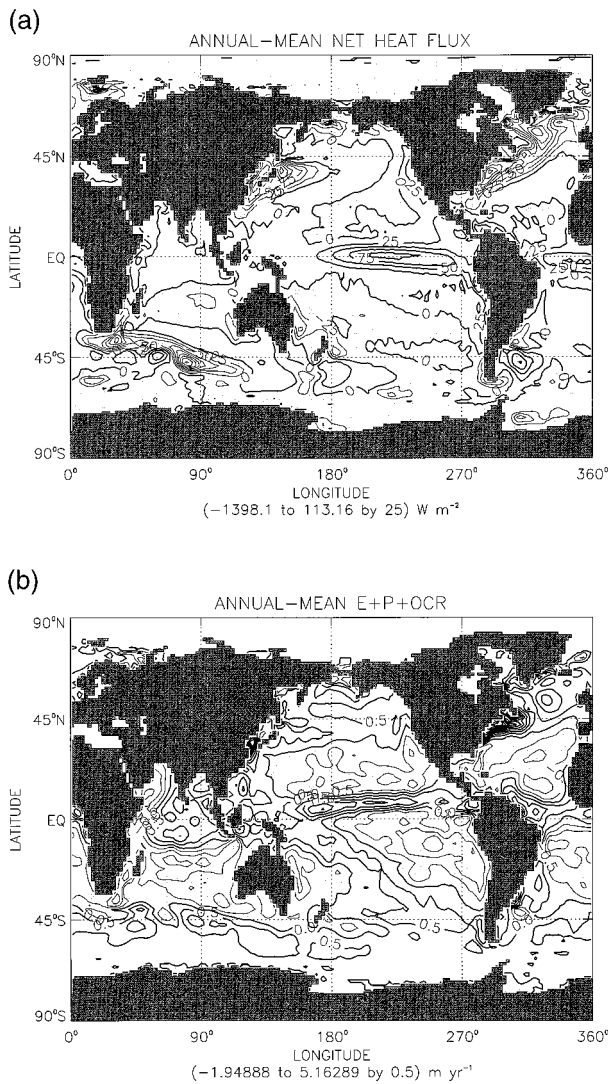


FIG. 14. (a) The average net heat flux into the ocean in W m^{-2} and (b) the average net freshwater flux into the ocean m yr^{-1} , excluding the strongly restored areas under sea ice.

equatorial Atlantic and Indian Oceans. The ocean loses freshwater in the evaporation zones of the subtropical oceans and in the Mediterranean. More information will be given in section 7 about the breakdown of the net freshwater flux into its various components given in Eq. (4).

The model northward heat and freshwater transports are shown in Fig. 15, along with several estimates from observations. The maximum northward transport is 1.6 PW at 21°N , which is smaller than the Trenberth and Solomon (1994) estimate of 2 PW. The model transport at 24°N is also smaller than the ocean estimate of Hall and Bryden (1982) and Bryden et al. (1991), although it is just within the observational error bar. Most of the northward transport in the model occurs in the Atlantic Ocean, which accounts for 1 PW of transport, and this agrees well with the Trenberth and Solomon estimate.

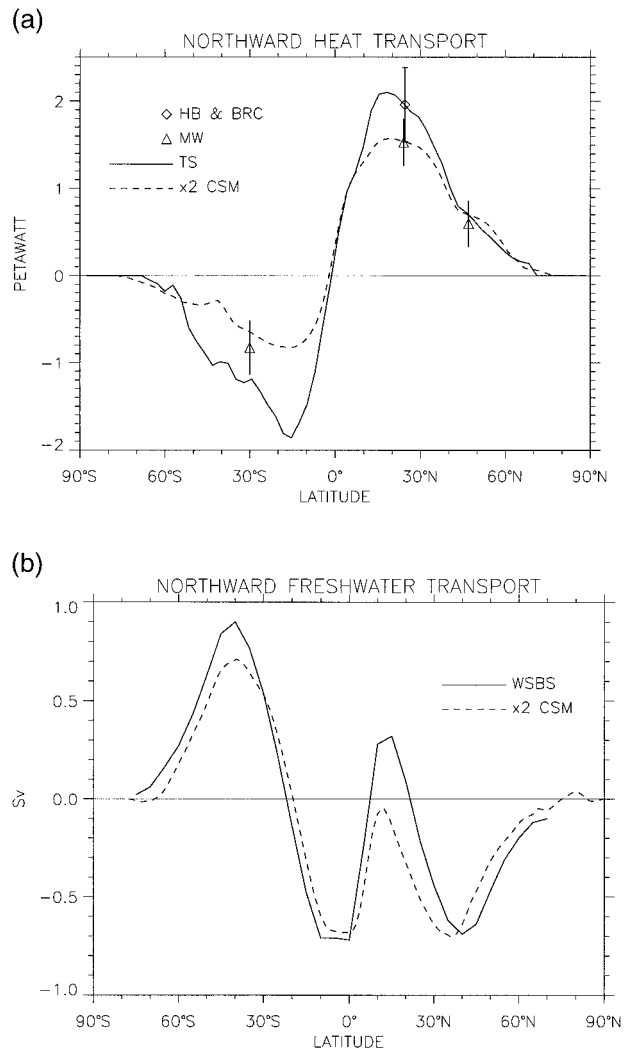


FIG. 15. (a) The global, zonally averaged northward heat transport in PW, and observational estimates from Trenberth and Solomon, Macdonald and Wunsch, Hall and Bryden, and Bryden et al. (b) The global, zonally averaged northward freshwater transport in Sverdrups and the observational estimate from Wijffels et al.

Thus, the model heat transport in the North Pacific is almost a factor of 2 smaller than the Trenberth and Solomon estimate. This is also the case for global poleward transport in the Southern Hemisphere, with the model maximum being 0.8 PW southward at 23°S . This discrepancy is larger than the Trenberth and Solomon error bar, so the model and this observational estimate are not in agreement. The smaller southward heat transport in the Southern Hemisphere has also recently been found in observational analyses (K. E. Trenberth 1997, personal communication). The CSM ocean heat transport agrees very well with the estimates from the global box inverse model of Macdonald and Wunsch (1996) at 48°N , 24°N , and 30°S .

The northward transport of freshwater is very difficult to estimate from observations, and the Wijffels et al.

(1992) estimate is shown Fig. 15b. Given this difficulty, the agreement between the model and observations is good. The major discrepancies are that the model does not transport any freshwater northward at about 10°N, and the model transport in the Southern Hemisphere is weaker than the Wijffels et al. (1992) estimate. The southward freshwater transport in the Northern Hemisphere is almost equally divided between the Atlantic and Indo-Pacific Oceans, and the Southern Hemisphere northward transport is dominated by the Indo-Pacific Ocean.

5. Large-scale potential vorticity

Potential vorticity is an important dynamical quantity in the theory of atmospheric and oceanic circulation because it is conserved following the flow in inviscid, adiabatic conditions. The inertial term in the momentum equation is very small away from fast currents in non-eddy-permitting models, such as the one described here. In this case, the relevant dynamical quantity is the large-scale potential vorticity defined by

$$Q = -\frac{f\rho_z}{\rho_0}, \tag{5}$$

where f is the Coriolis parameter, ρ is the potential density, and ρ_0 is a reference density. The mesoscale eddy parameterization described in section 2 is based on the idea that mixing in the ocean interior is mostly along isopycnal surfaces. This suggests that Q should be evaluated on surfaces of constant potential density.

Figure 16 shows a meridional section along 165°W in the Pacific of depth and Q plotted against potential density referenced to 4 km. It can be directly compared with Fig. 6 of O'Dwyer and Williams (1997), which shows the same quantities calculated from the original data used by Levitus et al. (1994). Figure 16a shows that the density surfaces are almost flat between 20°S and 20°N but deepen in both hemispheres between 30° and 40°. It also shows that the surfaces shoal dramatically across the ACC. O'Dwyer and Williams show a similar distribution, although the midlatitude domes are somewhat smaller and the thickness gradient is somewhat stronger in reality than in the model. This implies a weaker vertical density gradient in the model, which is consistent with the weaker vertical salinity gradient in the Pacific shown in Fig. 11d. Figure 16b shows that the model Q distribution is also quite similar to the observations with values reaching $\pm 100 \times 10^{-12} \text{ m}^{-1} \text{ s}^{-1}$ around 50°N and 50°S, and bottom ocean values ranging between $\pm 10 \times 10^{-12} \text{ m}^{-1} \text{ s}^{-1}$. Compared to O'Dwyer and Williams's Fig. 6, the ocean model has more uniform thicknesses between isopycnals and less variability in the Q distribution than the observational analysis. Gent et al. (1995) show that the eddy parameterization tends to produce flat isopycnals with uniform thickness between them. It is clear that this is the result in the deep model ocean. Comparison with observations

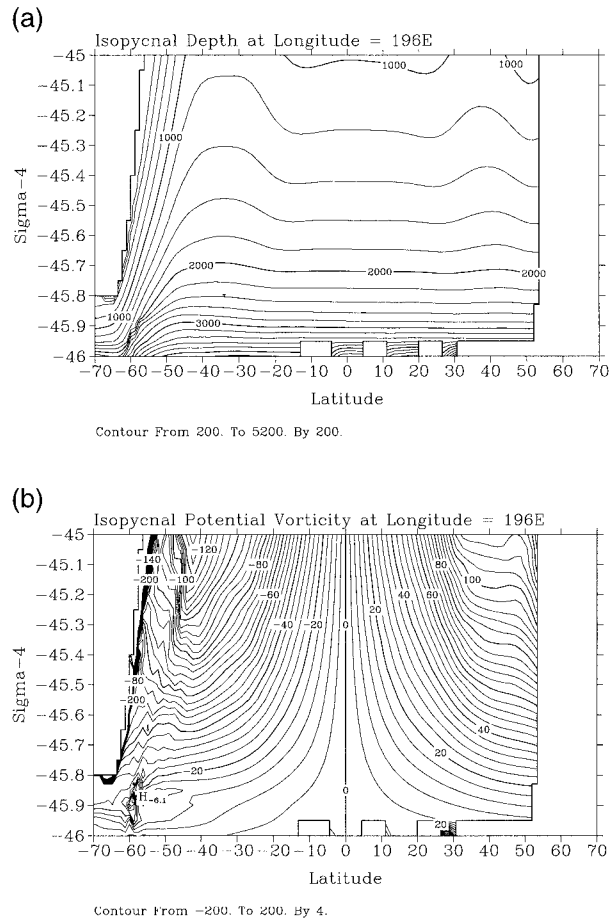


FIG. 16. Meridional section of (a) depth (km) and (b) potential vorticity ($\text{m}^{-1} \text{ s}^{-1}$) against potential density referenced to 4 km along 165°W in the model Pacific Ocean.

shows that the model isopycnals are more uniform than in reality, which suggests that the isopycnal mixing parameter κ_1 from Eq. (1) should vary with depth and have smaller values in the deep than in the upper ocean.

6. The annual cycle and deep water formation

Danabasoglu et al. (1996) show that the amplitude of the annual cycle is suppressed when the ocean model is integrated in accelerated mode. They then show that the annual cycle amplifies rapidly when the model is run synchronously, so that only a short synchronous integration is required. We ran the model synchronously for 15 yr and then for a further 2 yr to diagnose the annual cycle in the simulation.

The annual cycle in the NCEP reanalyzed wind stress is quite realistic and has been documented elsewhere. The maximum zonal wind stress in the ACC region varies from 0.24 N m^{-2} in July to 0.14 N m^{-2} in January. However, the annual cycle in the ACC is not that large, being about 10% of the annual mean value of 120 Sv. The variation in the wind stress over all the midlatitude

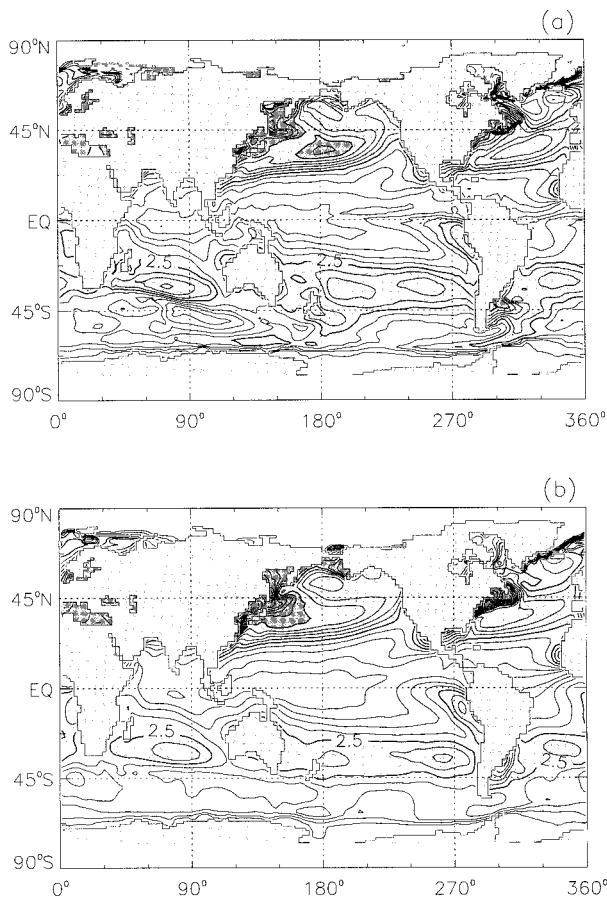


FIG. 17. The amplitude of the sea surface temperature annual harmonic ($^{\circ}\text{C}$). (a) The model and (b) the climatology of Shea et al.

oceans is large between winter and summer, and this causes a large annual cycle in the strength of the midlatitude gyres. For example, the gyre strength in the North Pacific varies by about 30%, being 44 Sv in January and 32 Sv in July. The subpolar gyre in the North Pacific, which occurs mostly poleward of 45°N , also has a large annual cycle. However, the annual cycle of the barotropic streamfunction is difficult to compare with observations, both because observations are sparse and because these midlatitude gyres are considerably weaker than reality because of the coarse model resolution.

A much better observed ocean quantity is SST. The ocean model SST is strongly constrained by the imposed atmospheric temperature, but Fig. 17 shows the amplitude of the annual harmonic calculated from the model SST and from the climatology of Shea et al. (1990). In general, the patterns are very similar, although the observed field is somewhat smoother than the model field. At most locations, the amplitude of the model annual cycle is larger than the Shea et al. value, but the reverse is true in the equatorial Indian Ocean and in a region of the ACC between 80° and 120°E . The model has a stronger annual cycle in the midlatitude gyres with larger regions where the amplitude is $>3^{\circ}\text{C}$ in all three

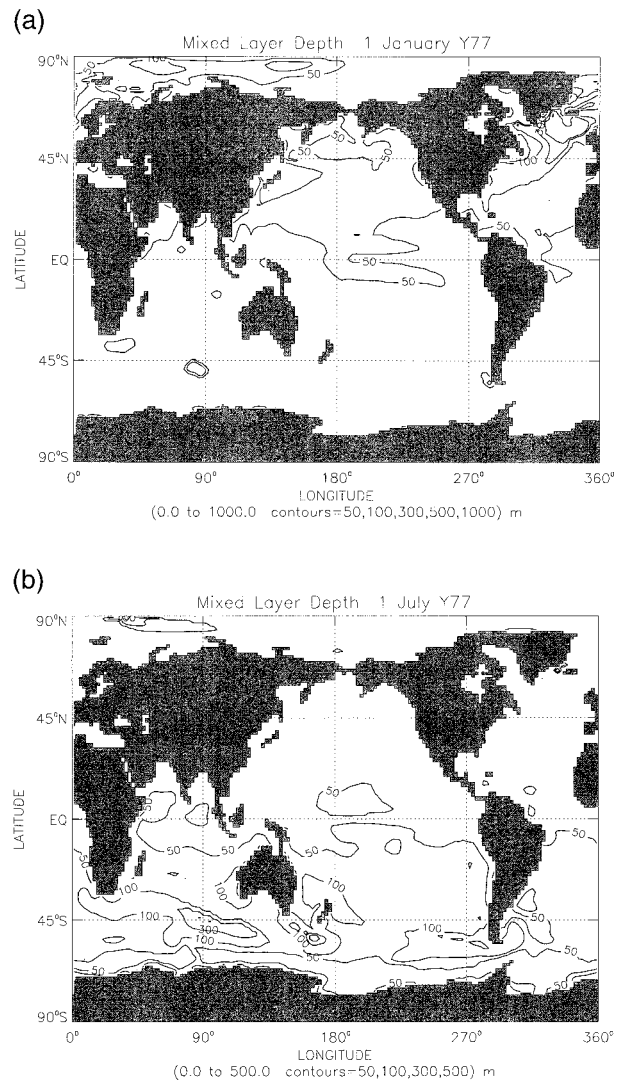


FIG. 18. Mixed layer depth (m) in the last year of the model spinup run: (a) 1 January and (b) 1 July. Values greater than 300 m are shaded.

southern oceans and larger regions $>4^{\circ}\text{C}$ in both Northern Hemisphere oceans. This overestimation of the annual cycle could be due in part to the fact that the ocean model does not resolve the diurnal cycle. Tests where the solar heating is modified according to the time of day show enhanced mixing in the KPP boundary layer scheme at night, and this leads to a reduction in the amplitude of the model annual cycle.

However, the KPP boundary layer scheme does a good job resolving the annual cycle in the model. This has been analyzed much more thoroughly in the $\times 3$ simulation and is described in the companion paper by Large et al. (1997). Figure 18 shows values of the mixed layer depth from the last year of the model spinup for 1 January and 1 July. The mixed layer depth in the summer hemisphere is <50 m almost everywhere and can often reach its minimum allowed depth of 6.25 m,

which is half the depth of the first model level. In the winter hemisphere, the mixed layer depth is >100 m in the western midlatitude gyres. On 1 January, the largest values are in the north Atlantic Ocean and the Labrador Sea. The greatest depth is >1500 m west of Iceland. These are the regions where deep water formation occurs in the model, although more deep water should be formed north of Iceland and spill over the Denmark Strait and the Iceland–Faeroe Ridge. On 1 July, the largest values occur at scattered locations in the ACC region, with the greatest depth just south of New Zealand.

7. Solution sensitivities

In this section, we discuss some solution sensitivities, especially to the freshwater forcing and model resolution. The equilibrium solution is sensitive to many other choices made, which are not fully discussed here. For example, the ocean circulation obtained depends upon the choices of viscosity and diffusivity, but this has been discussed previously by Bryan (1987), Danabasoglu and McWilliams (1995), and others. The thermohaline circulation obtained is somewhat sensitive to the timescale of the strong restoring flux fields of θ and S under sea ice. This is documented fully in the $\times 3$ model resolution version in Large et al. (1997); a similar sensitivity is expected for the $\times 2$ model.

We have mentioned already how sensitive the equilibrium solution is to the freshwater forcing because of the lack of a feedback effect of the surface salinity except on very long timescales. This first became very obvious in trying to obtain an equilibrium $\times 3$ solution. It took many integrations and many false starts before the freshwater forcing given by Eq. (4) and the method of updating the precipitation factor f were decided upon. In the $\times 3$ solution described in Large et al. (1997), the coefficient Γ_F corresponds to an open-ocean salinity restoring timescale of 2 yr over 50 m. We first tried to integrate the $\times 2$ version using the interpolated $\times 3$ solution as the initial condition, with Γ_F corresponding to 2 yr. The model was run for more than 100 surface tracer years in accelerated mode. The SST equilibrated very quickly because of the strong negative feedbacks of SST on the heat flux. There were trends in the layer average values of θ with cooling in the upper 25 layers above 1 km and warming in the bottom 20 layers below 1 km. However, these trends were very weak, and there was little change in the globally averaged value of θ from its initial value. This can be contrasted with the trends in salinity. The upper ocean above 1 km was getting fresher while the ocean below 1 km was getting saltier, and the trends were strong. These trends were taking the $\times 2$ solution farther from the Levitus (1982) observations than the $\times 3$ solution, with no sign of the linear trends weakening at the end of the integration. By the end of the integration, the global average sea surface salinity had decreased by 0.07 ppt to 34.58 ppt

and the volume average salinity had increased by >0.04 ppt. Over this integration, the magnitude of the global averaged restoring term $\langle F_w \rangle$ in Eq. (4) increased by almost a factor of 2 from 20 to $38 \text{ kg m}^{-2} \text{ s}^{-1}$ and was still increasing. This suggested that the $\times 2$ model required a larger open-ocean salinity restoring term than the $\times 3$ model and that a larger value of Γ_F should be used. Eventually, a value four times larger for the $\times 2$ version, corresponding to a restoring timescale of 6 months over 50 m, was chosen because then the θ and S fields showed very little trend, so that the equilibrium $\times 2$ and $\times 3$ solutions are quite similar.

The MSU monthly estimates of precipitation from Spencer (1993) have quite large error estimates, which is why we felt free to multiply them by the factor f and include the local salinity restoring term. One could argue that the precipitation field P' that the model needs to maintain this equilibrium solution is given by

$$P' = fP + F_w - \langle F_w \rangle. \quad (6)$$

Of course, this assumes that there is no error in the model evaporation and advection and that marginal sea inputs and river runoff are well represented by F_w . This is made more obvious because the P' field defined in Eq. (6) is negative in a few locations, although the values are very close to zero. Anyway, it is instructive to compare the annual average P field, shown in Fig. 19a, with the annual average P' field, defined by Eq. (6), from the model shown in Fig. 19b. The heaviest rainfall in the Pacific intertropical convergence zone is moved westward to the date line in the P' field compared to the 130°W in the MSU data. The maximum in the South Pacific convergence zone is moved slightly eastward in P' , and the maxima in the Indian Ocean are moved westward in the P' field. The reasons for these differences in P and P' are not clear, but other strong features in the P' field can be explained. There are large maxima at the mouths of several major rivers where the salinity errors shown in Fig. 9b are large due to the lack of river runoff in the freshwater forcing. The large values west of Japan, east of the United States, and in the Southern Hemisphere around 45°S are all regions of large net ocean heat loss (see Fig. 14a) and SST error (see Fig. 9a). When the SST is too large, probably due to model advection errors, then the latent heat loss and the model evaporation will also be too large. The restoring term will tend to balance this evaporation locally, leading to large values in the P' term. The P' field in Fig. 19b is considerably different from the MSU precipitation data in Fig. 19a, which says that the local salinity restoring term in Eq. (4) is significant, even though the restoring time is 6 months. This is emphasized by the fact, mentioned above, that an integration with a 2-yr restoring time led to large model salinity errors. Thus, the lack of a surface salinity feedback leads to a strong sensitivity of the equilibrium salinity field to the freshwater forcing.

Another very important question is, what is the sen-

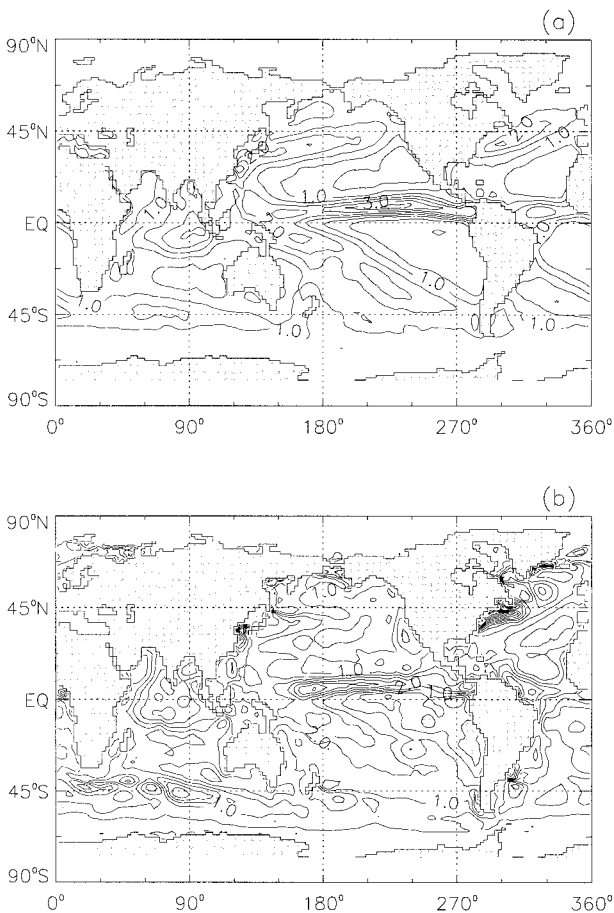


FIG. 19. (a) The annual average precipitation field from Spencer (m yr^{-1}) and (b) the annual average P' field from the model; see Eq. (6).

sitivity of the equilibrium global ocean solutions to the model resolution chosen? Surprisingly, there are rather few studies addressing this question, especially with coarse-resolution global ocean models that typically have been used in coupled model climate studies. However, Covey (1995) reports on a study of this kind. He ran a z -coordinate model with the standard physics and forcing of a few years ago, namely, strong horizontal tracer mixing, no boundary layer scheme, centered advection by the Eulerian velocity only, and surface boundary conditions of strong restoring to Levitus θ and S everywhere. In addition, he used quite strong restoring of θ and S to the Levitus values in the ocean below about 700 m, because this had already been done in the higher-resolution cases. He used resolutions ranging from 4° to $1/4^\circ$ and plotted the northward heat transport in these cases in his Fig. 10. It shows a very strong dependence of the northward heat transport on model resolution, both in the global ocean and in the Atlantic Ocean and there is no hint of convergence of this important climate quantity with increasing resolution. The figure also shows a strong sensitivity to two cases with $1/2^\circ$ resolution, one run with Laplacian momentum dif-

fusion and one run with biharmonic diffusion. More recently, Fanning and Weaver (1997) have run a model with standard physics both in ocean-alone mode and coupled to a simple atmospheric model. The ocean model resolution varied between 4° and $1/4^\circ$. Again, there were significant changes with model resolution in important climate quantities such as the northward heat transport.

The $\times 3$ equilibrium solution described in Large et al. (1997) and the $\times 2$ equilibrium solution documented here have very similar annually averaged fields. The barotropic streamfunction in Fig. 2 does have somewhat stronger midlatitude gyres than its $\times 3$ counterpart, but the ACC has very similar magnitude in the two solutions. The strength of the thermohaline circulation in the $\times 2$ model is only slightly stronger than that in the $\times 3$, and there are only small differences in the global θ and S fields in the two versions. Certainly, the difference between the two solutions is much smaller than the errors of either compared to the Levitus (1982) climatology. The two resolutions also give rather similar net heat and freshwater flux fields, shown in Fig. 14 for the $\times 2$ resolution. Even so, the two solutions have somewhat different northward heat transports, which are shown in Fig. 20a. In the Northern Hemisphere, the transports are almost the same because the thermohaline circulation in the North Atlantic, which accounts for nearly all the heat transport, is very similar in the two solutions. However, in the Southern Hemisphere the transports are significantly different, with the $\times 2$ solution having a maximum of 0.75 PW, whereas the $\times 3$ solution has a maximum of 1.12 PW. The transports in the two resolutions converge again at 60°S . Also shown in Fig. 20a is the implied ocean heat transport from CCM3 run at T42 resolution with observed SST values. In the Northern Hemisphere, the ocean model values are considerably smaller than the CCM3 implied transport, but in the Southern Hemisphere, the $\times 2$ model transport agrees quite well with the CCM3 implied transport. Two conclusions can be drawn, however. First, the dependence of northward heat transport on model resolution in the NCAR CSM ocean model is much reduced compared to that shown by Covey (1995). Second, the heat transport in the $\times 2$ ocean and the implied heat transport in CCM3 are quite close, so that the two components are very compatible in this respect. This has not been true in the past because, for example, Gleckler et al. (1995) show that most atmospheric GCMs implied an equatorward heat transport for the ocean in the Southern Hemisphere. This was the case for the previous version of the atmospheric model, CCM2, and CCM3 is much improved in this important measure.

Figure 20b shows the northward freshwater transport in the $\times 2$ and $\times 3$ models and the implied global freshwater transport from CCM3 run at T42 resolution with observed SST values. The freshwater transport in the two model resolutions are quite similar, so again there

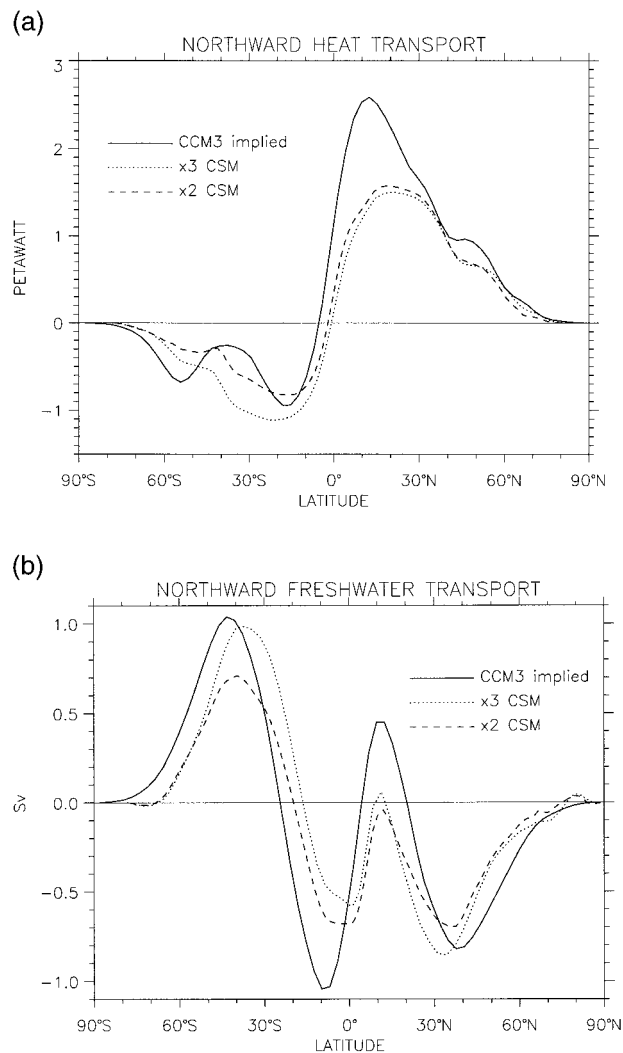


FIG. 20. The global, zonally averaged northward transports from the $\times 2$ and $\times 3$ model versions, and the implied transports from the CCM3 atmosphere model run at T42 with observed SST values. (a) Northward heat transport in PW, and (b) northward freshwater transport (Sv).

is not a large dependence of this transport on the model resolution, which is rather encouraging. The CCM3 estimate includes precipitation over land, in order to have a closed budget. A river runoff model would be needed to get the true implied ocean transport. Even so, the pattern from the CCM3 estimate is quite close to the ocean model transport, but the magnitude of the CCM3 estimate is about 20% larger than the $\times 2$ model transport.

8. Conclusions

The Oceanography Section has provided and documented the global ocean component of the NCAR Climate System Model. It has many improvements over previous noneddy-permitting global ocean models. The

most important are parameterizations of the effects of mesoscale eddies, an improved upper boundary layer, an improved numerical advection scheme, and an improved method of forcing ocean-alone calculations. This results in a much better equilibrium solution, especially in properties important for climate, compared to ocean observations than previous ocean models of the genre.

There are, of course, still obvious and important errors in the equilibrium solution that reflect model deficiencies. The most obvious is in the Atlantic Ocean, where the overturning circulation does not go deep enough and Antarctic bottom water fills too much of the deep Atlantic Ocean. This is likely due to a combination of factors. It is known that z -coordinate models do a poor job representing flows along steep topography, whereas models using coordinates more aligned along the topography behave much better. The regions where deep water is formed in the North Atlantic in this model are sensitive to the surface forcings used to drive it. In this simulation, more deep water is formed south of Iceland than north of it in the Greenland-Iceland-Norwegian Sea. This also occurs in the $\times 3$ model solution described in Large et al. (1997), but the precise sensitivity of this to both horizontal and vertical model resolution remains to be found. The freshwater flux still needs a restoring to observations term in order to obtain a stable salinity distribution. Would this still be necessary if the model explicitly took account of river runoff? The model also strongly restores to observations under sea ice, and this could be eliminated if the ocean was integrated with an active sea-ice model. These sensitivities and model improvements remain to be explored in the future as the ocean component of the NCAR Climate System Model is further improved.

Acknowledgments. We would like to thank Julianna Chow, Jan Morzel, and Nancy Norton, who are software engineers in the NCAR Oceanography Section and did much of the work to produce the CSM global ocean component. Thanks also to the ocean group at the Geophysical Fluid Dynamics Laboratory who produced and maintained the MOM code on which this model is based. Gokhan Danabasoglu and Jan Morzel were supported by the NOAA Office of Global Programs under Grant NA56GP0246.

REFERENCES

- Bryan, F. O., 1987: Parameter sensitivity of primitive equation ocean general circulation models. *J. Phys. Oceanogr.*, **17**, 970–985.
- Bryan, K., 1984: Accelerating the convergence to equilibrium of ocean–climate models. *J. Phys. Oceanogr.*, **14**, 666–673.
- Bryden, H. L., D. H. Roemmich, and J. A. Church, 1991: Ocean heat transport across 24°N in the Pacific. *Deep-Sea Res.*, **38**, 297–324.
- Covey, C., 1995: Global ocean circulation and equator–pole heat transport as a function of ocean GCM resolution. *Climate Dyn.*, **11**, 425–437.
- Cox, M. D., 1987: Isopycnal diffusion in a z -coordinate ocean model. *Ocean Modelling* (unpublished manuscript), **74**, 1–5.

- Danabasoglu, G., and J. C. McWilliams, 1995: Sensitivity of the global ocean circulation to parameterizations of mesoscale tracer transports. *J. Climate*, **8**, 2967–2987.
- , —, and P. R. Gent, 1994: The role of mesoscale tracer transports in the global ocean circulation. *Science*, **264**, 1123–1126.
- , —, and W. G. Large, 1996: Approach to equilibrium in accelerated global oceanic models. *J. Climate*, **9**, 1092–1110.
- Fanning, A. F., and A. J. Weaver, 1997: A horizontal resolution and parameter sensitivity study of heat transport in an idealized coupled climate model. *J. Climate*, **10**, 2469–2479.
- Farrow, D. E., and D. P. Stevens, 1995: A new tracer advection scheme for Bryan and Cox type ocean general circulation models. *J. Phys. Oceanogr.*, **25**, 1731–1741.
- Gent, P. R., and J. C. McWilliams, 1990: Isopycnal mixing in ocean circulation models. *J. Phys. Oceanogr.*, **20**, 150–155.
- , J. Willebrand, T. J. McDougall, and J. C. McWilliams, 1995: Parameterizing eddy-induced tracer transports in ocean circulation models. *J. Phys. Oceanogr.*, **25**, 463–474.
- Gerdes, R., C. Köberle, and J. Willebrand, 1991: The influence of numerical advection schemes on the results of ocean general circulation models. *Climate Dyn.*, **5**, 211–226.
- Gleckler, P. J., and Coauthors, 1995: Cloud–radiative effects on implied oceanic energy transports as simulated by atmospheric general circulation models. *Geophys. Res. Lett.*, **22**, 791–794.
- Hall, M. M., and H. L. Bryden, 1982: Direct estimates and mechanisms of ocean heat transport. *Deep-Sea Res.*, **29**, 339–359.
- Hecht, M. W., W. R. Holland, and P. J. Rasch, 1995: Upwind-weighted advection schemes for ocean tracer transport: An evaluation in a passive tracer context. *J. Geophys. Res.*, **100**, 763–20 778.
- Holland, W. R., J. C. Chow, and F. O. Bryan, 1998: Application of a third-order upwind scheme in the NCAR ocean model. *J. Climate*, **11**, 1487–1493.
- Holtlag, A. A. M., E. I. F. de Bruijn, and H.-L. Pan, 1990: A high resolution air mass transformation model for short-range weather forecasting. *Mon. Wea. Rev.*, **118**, 1561–1565.
- Kalnay, E., and Coauthors, 1996: The NCEP/NCAR 40-year reanalysis project. *Bull. Amer. Meteor. Soc.*, **77**, 437–471.
- Large, W. G., J. C. McWilliams, and S. C. Doney, 1994: Oceanic vertical mixing: A review and a model with a nonlocal boundary layer parameterization. *Rev. Geophys.*, **32**, 363–403.
- , G. Danabasoglu, S. C. Doney, and J. C. McWilliams, 1997: Sensitivity to surface forcing and boundary layer mixing in the NCAR CSM ocean model: Annual-mean climatology. *J. Phys. Oceanogr.*, **27**, 2418–2447.
- Ledwell, J. R., A. J. Watson, and C. S. Law, 1993: Evidence for slow mixing across the pycnocline from an open-ocean tracer release experiment. *Nature*, **364**, 701–703.
- Lee, T., and J. Marotzke, 1997: Inferring meridional mass and heat transports of the Indian Ocean by fitting a general circulation model to climatological data. *J. Geophys. Res.*, **102**, 585–10 602.
- Leonard, B. P., 1979: A stable and accurate convective modeling procedure based on quadratic upstream interpolation. *Comput. Meth. Appl. Eng.*, **19**, 59–98.
- Levitus, S., 1982: *Climatological Atlas of the World Ocean*. NOAA Prof. Paper 13, National Oceanic and Atmospheric Administration, 173 pp.
- , R. Burgett, and T. P. Boyer, 1994: *Salinity*. Vol. 3, *World Ocean Atlas 1994*, National Oceanic and Atmospheric Administration, 99 pp.
- Macdonald, A. M., and C. Wunsch, 1996: An estimate of global ocean circulation and heat fluxes. *Nature*, **382**, 436–439.
- Molinari, R. L., R. A. Fine, and E. Johns, 1992: The deep western boundary current in the tropical North Atlantic Ocean. *Deep-Sea Res.*, **39**, 1967–1984.
- NCAR Oceanography Section, 1996: The NCAR CSM ocean model. NCAR Tech. Note NCAR/TN-423+STR, 75 pp. [Available from NCAR, P.O. Box 3000, Boulder, CO 80307.]
- O'Dwyer, J., and R. G. Williams, 1997: The climatological distribution of potential vorticity over the abyssal ocean. *J. Phys. Oceanogr.*, **27**, 2488–2506.
- Redi, M. H., 1982: Oceanic isopycnal mixing by coordinate rotation. *J. Phys. Oceanogr.*, **12**, 1154–1158.
- Rossow, W. B., and R. A. Schiffer, 1991: ISCCP cloud data products. *Bull. Amer. Meteor. Soc.*, **72**, 2–20.
- Shea, D. J., K. E. Trenberth, and R. W. Reynolds, 1990: A global monthly sea surface temperature climatology. NCAR Tech. Note NCAR/TN-345, 167 pp. [Available from NCAR, P.O. Box 3000, Boulder, CO 80307.]
- Sloss, P. W., 1988: Digital relief of the surface of the Earth. Data Announcement 88-MGG-02, 50 pp. [Available from National Geophysical Data Center, 325 Broadway, Boulder, CO 80303.]
- Spencer, R. W., 1993: Global oceanic precipitation from the MSU during 1979–91 and comparisons to other climatologies. *J. Climate*, **6**, 1301–1326.
- Trenberth, K. E., and A. Solomon, 1994: The global heat balance: Heat transports in the atmosphere and ocean. *Climate Dyn.*, **10**, 107–134.
- Troen, I. B., and L. Mahrt, 1986: A simple model of the atmospheric boundary layer; Sensitivity to surface evaporation. *Bound.-Layer Meteor.*, **37**, 129–148.
- Wajsovicz, R. C., 1993: A consistent formulation of the anisotropic stress tensor for use in models of the large scale ocean circulation. *J. Comput. Phys.*, **105**, 333–338.
- Webb, D. J., 1995: The vertical advection of momentum in Bryan–Cox–Semtner ocean general circulation models. *J. Phys. Oceanogr.*, **25**, 3186–3195.
- Wijffels, S. E., R. W. Schmitt, H. L. Bryden, and A. Stigebrandt, 1992: Transport of freshwater by the oceans. *J. Phys. Oceanogr.*, **22**, 155–162.